EOS-ESTM: a flexible climate model for habitable exoplanets

L. Biasiotti [1,2]* P. Simonetti [1,2] G. Vladilo,[1] L. Silva [1,3] G. Murante [1] S. Ivanovski,[1] M. Maris,[1] S. Monai,[1] E. Bisesi,[1] J. von Hardenberg[4] and A. Provenzale[5]

[1]*INAF – Trieste Astronomical Observatory, Via G. B. Tiepolo 11, I-34143 Trieste, Italy*
[2]*Department of Physics, University of Trieste, Via G. B. Tiepolo 11, I-34143 Trieste, Italy*
[3]*IFPU – Institute for Fundamental Physics of the Universe, Via Beirut 2, I-34014 Trieste, Italy*
[4]*Politecnico di Torino - DIATI, Corso Duca degli Abruzzi 24, I-10129 Torino, Italy*
[5]*Institute of Geosciences and Earth Resources – IGG, National Research Council of Italy, I-56127 Pisa, Italy*

ABSTRACT

Rocky planets with temperate conditions provide the best chance for discovering habitable worlds and life outside the Solar system. In the last decades, new instrumental facilities and large observational campaigns have been driven by the quest for habitable worlds. Climate models aimed at studying the habitability of rocky planets are essential tools to pay off these technological and observational endeavours. In this context, we present EOS-ESTM, a fast and flexible model aimed at exploring the impact on habitability of multiple climate factors, including those unconstrained by observations. EOS-ESTM is built on ESTM, a seasonal-latitudinal energy balance model featuring an advanced treatment of the meridional and vertical transport. The novel features of EOS-ESTM include: (1) parametrizations for simulating the climate impact of oceans, land, ice, and clouds as a function of temperature and stellar zenith distance and (2) a procedure (EOS) for calculating the radiative transfer in atmospheres with terrestrial and non-terrestrial compositions illuminated by solar- and non-solar-type stars. By feeding EOS-ESTM with Earth's stellar, orbital, and planetary parameters, we derive a reference model that satisfies a large number of observational constraints of the Earth's climate system. Validation tests of non-terrestrial conditions yield predictions that are in line with comparable results obtained with a hierarchy of climate models. The application of EOS-ESTM to planetary atmospheres in maximum greenhouse conditions demonstrates the possibility of tracking the snowball transition at the outer edge of the HZ for a variety of planetary parameters, paving the road for multiparametric studies of the HZ.

Key words: astrobiology – planets and satellites: atmospheres – planets and satellites: terrestrial planets.

1 INTRODUCTION

Over the past two decades, ground- and space-based observations have unveiled thousands of exoplanets and planetary systems around other stars in our Galaxy. About 4900 exoplanets are currently confirmed,[1] in large part detected as transits by the *Kepler*[2] mission (Borucki et al. 2010). Its successor TESS[3] (*Transit Exoplanet Survey Satellite*; Ricker et al. 2015) is expected to boost the detection number, while CHEOPS[4] (*CHaracterizing ExOPlanet Satellite*; Broeg, Benz & Fortier 2018) will help to characterize the structural properties of already selected planets. In the short term, PLATO[5] (*PLAnetary Transits and Oscillations of stars*; Rauer et al. 2014) will search transiting Earth analogues around bright stars.

The statistically relevant numbers of detected planets are allowing to investigate on all aspects of planetary structure and formation in different size ranges, as a function of stellar spectral type, composition, and even stellar multiplicity. A diversity of planetary system architectures and a large range of planetary masses and/or radii have been observed, showing that the Solar system is just one possible outcome of the planetary formation process (e.g. Udry & Santos 2007; Howard et al. 2012; Winn & Fabrycky 2015; Kaltenegger 2017). Observations are necessarily biased towards giant gaseous planets around late-type stars, but the ever increasing statistics has allowed to infer that virtually any star in our Galaxy hosts at least one planet, with the planetary size distribution suggesting a steep increase towards small rocky Earth-like planets with thin atmospheres. In fact, while it has been found that planetary masses offer a loose constraint on composition, currently in all cases it has been found that at small radii, $R_p \leq 1.5 - 2$ R$_\oplus$, all planets are rocky (e.g. Rogers 2015) with a gap, i.e. an almost sudden transition, between Earth-like volatile poor and Neptune-like volatile rich planets (e.g. Fulton et al. 2017).

These studies are shifting the current research from detection and statistics to full characterization of planetary properties, with one of the main goals of exoplanetary science being the quest for life outside the Solar system. This endeavour can only be tackled through remote atmospheric spectroscopy (transit, reflection, emission, and their time variations; e.g. Kreidberg 2018) of potentially habitable rocky planets, in order to identify spectral features of biological origin.

[1]e.g. https://exoplanets.nasa.gov/; https://exoplanetarchive.ipac.caltech.edu/
[2]https://www.nasa.gov/mission_pages/kepler/main/index.html
[3]https://tess.mit.edu/
[4]https://www.esa.int/Science_Exploration/Space_Science/Cheops
[5]https://sci.esa.int/web/plato/

This possibility rests on the notion that the metabolic activity by-products for a well developed surface life may impact the atmospheric chemistry to a measurable amount (e.g. Lovelock 1965; Kasting et al. 2014).

This observational challenge (e.g. Fujii et al. 2018, for a review) should be partly within reach of the recently launched *JWST* (*James Webb Space Telescope*; Gardner et al. 2006; Kalirai 2018), probably limited to nearby M-type stars (e.g. Koll et al. 2019), and, within the next decade, of the approved spatial mission ARIEL[6] (*Atmospheric Remote-sensing Infrared Exoplanet Large-survey*; Tinetti et al. 2018), although mainly for objects with warm H-dominated atmospheres. Nearby terrestrial analogues are expected to be detected with the ground-based E-ELT[7] (Snellen et al. 2015; Morley et al. 2017) equipped with the spectrograph HIRES (Maiolino et al. 2013). In the longer term, further space-based projects currently under assessment will be selected that specifically aim to directly detect and characterize nearby temperate terrestrial analogues, e.g. HabEX[8] (*Habitable Exoplanet Observatory*; Gaudi et al. 2020), LUVOIR[9] (*Large UV/Optical/IR Surveyor*; The LUVOIR Team 2019), OST[10] (*Origins Space Telescope*; Wiedner et al. 2021), LIFE[11] (*Large Interferometer For Exoplanets*; Quanz et al. 2021). The recent decadal survey for astronomy and astrophysics (Astro2020) report[12] endorsed recommendations for a single UV/optical/IR flagship mission that picks a compromise concept between LUVOIR and HabEX.

To accomplish the demanding task of searching for and deciphering spectral signatures, a thorough and holistic observational and theoretical characterization of carefully selected rocky exoplanets is required. The selection, among the observationally reachable targets for high-resolution spectroscopy of thin atmospheres, requires habitability studies with climate models. These simulations will enable the identification of those exoplanets with the largest chance of potentially hosting a surface diffuse life, i.e. with the largest habitability, that must be evaluated over a wide range of mostly unknown conditions. Moreover, the interpretation of any detected atmospheric features in terms of physical status of the atmosphere, and of their biotic or abiotic origin, will be unavoidably subjected to huge uncertainties and degeneracies, including false positives even for oxygen (e.g. Meadows & Barnes 2018; Schwieterman et al. 2018). A considerable effort of modellization that exploits all available observations will be needed in order to assess the global physical characterization of the selected exoplanets, and in particular precisely of their potential surface climate and habitability.

Habitability studies for exoplanets rely on the concept of the habitable zone (HZ), classically defined as the range of stellar insolation, the main driver of climate, that allows surface temperatures compatible with a long-term presence of surface liquid water for a planet with an N_2-CO_2-H_2O atmosphere and a climate system stabilized by the carbonate-silicate feedback (Walker, Hays & Kasting 1981; Kasting, Whitmire & Reynolds 1993; Kopparapu et al. 2013a, 2014). In these reference works, the inner and outer edges of the HZ are defined, respectively, for a H_2O- and a CO_2-dominated atmosphere, for an otherwise Earth-like planet orbiting stars of different spectral types. The HZ is considered as the prerequisite

for potentially inhabited planets with exchange of gases between the biosphere and atmosphere (Kasting et al. 2014; Schwieterman et al. 2018) and therefore for spectroscopic biosignature searches. Actually, in addition to insolation and spectral type, a large range of (mostly unknown) climate forcing factors affects planetary surface temperature and habitability, e.g. atmospheric mass and composition, surface gravity, radius, rotation period, obliquity, geography (e.g. Ramirez et al. 2019), in addition to the observable orbital parameters. Also, different definitions of habitability could be envisaged and calculated for an optimal selection of exoplanets.

The large variety of planetary situations, expected and already uncovered by observations hints that a large range of non-Earth conditions should be accounted for. The majority of these parameters can currently only be explored with climate simulations. Currently ∼60 observed rocky exoplanets are considered potentially habitable,[13] but their number may change should a multiparametric analysis of the huge possible parameter space of surface temperature be performed.

The climate and the surface habitability of exoplanets can be explored, as for the Earth, using a hierarchy of models, depending on the aim and problem to be addressed (see e.g. Shields 2019, for a review). Climate models should be able to account for, even at different levels of simplification, the complexity of the climate system due to the interplay of different components and processes, giving rise to feedbacks leading to multiple equilibria or even runaway conditions (Provenzale 2013). For instance, the water vapour and the ice/albedo feedbacks set the spatial and temporal limits of the liquid water HZ. The accounting of these complexities is particularly important to simulate conditions not treated in Earth-tailored climate models.

Fully coupled ocean-atmosphere General Circulation Models (GCM) are the most detailed and computing resources consuming models, in principle requiring a large amount of information to obtain meaningful results (e.g. detailed geography and orography). In fact GCM are often applied for exoplanetary studies by adopting an Earth or simplified configurations, such as an aquaplanet (e.g. Leconte et al. 2013; Wolf & Toon 2013, 2015; Shields et al. 2014; Kaspi & Showman 2015; Wolf et al. 2022). They are fundamental tools to compute the coupled atmospheric-ocean dynamics on the long term and to study atmospheric dynamics in particularly complex configurations. These include rocky planets in the HZ of M-type stars, the most numerous and easiest targets for spectroscopy follow-ups. Due to their proximity to the host stars, these planets are expected to be tidally locked into synchronous rotation (Leconte et al. 2015; Barnes 2017). GCM are also fundamental benchmarks for faster lower complexity models, allowing multiparametric simulations.

Among such simpler models, 1D single-column radiative-convective models including detailed line-by-line radiative transfer (RT) have been used for instance to define the reference classical HZ mentioned above. Another class of 1D models are the so-called zonal Energy Balance Models (EBM), which solve a latitudinally averaged energy balance with a simplified meridional heat diffusion equation (North, Cahalan & Coakley 1981; Spiegel, Menou & Scharf 2008). This class of models is still applied to the Earth climate, to be able to explore and isolate the effects of specific processes on the global climate (see e.g. Pierrehumbert 2010). Their flexibility and short computing time can be exploited also for the large parameter

---

[6]https://arielmission.space/; https://sci.esa.int/web/ariel/

[7]https://elt.eso.org/

[8]https://www.jpl.nasa.gov/habex/

[9]https://asd.gsfc.nasa.gov/luvoir/

[10]https://origins.ipac.caltech.edu/

[11]https://www.life-space-mission.com/

[12]https://nap.nationalacademies.org/catalog/26141/pathways-to-discovery-in-astronomy-and-astrophysics-for-the-2020s

[13]https://phl.upr.edu/projects/habitable-exoplanets-catalog, where the reported number refer to the empirical liquid water HZ, as defined by the insolation range received by Venus and Mars respectively ∼1 and 4 Gyr ago, when they could have hosted surface liquid water (Kasting et al. 1993).

space required to simulate exoplanetary conditions, by properly modelling all the terms entering the energy balance equation. By coupling single-column RT atmospheric modelling with an EBM (e.g. Williams & Kasting 1997; Vladilo et al. 2013; Haqq-Misra & Hayworth 2022, hereafter WK97 and V13, respectively), and by further elaborating a physically based description of the meridional transport, Vladilo et al. (2015, hereafter V15) developed a 2D EBM, the Earth-like planet surface temperature model (ESTM), specifically aiming to compute the seasonal and zonal surface temperature of non-tidally locked exoplanets with a large range of non-terrestrial (atmospheric and planetary) physical conditions. The range of applicability of this model was thoroughly explored in V15 by comparing with the 3D aquaplanet model by Kaspi & Showman (2015). The flexibility and fast computing time of ESTM has been exploited in Murante et al. (2020)[14] for a statistical study of the multiple equilibrium states affecting climate systems due to non-linear feedbacks (e.g. the warm and snowball Earth states, during the latter the Earth would have been tagged as non-habitable). In Silva et al. (2017b), we performed with ESTM a multiparametric exploration of the habitability for Kepler-452b (Jenkins et al. 2015), currently the only known Earth-twin candidate. ESTM, by computing the latitude- and seasonal-dependent surface temperature, allows different operative definitions of habitability to be computed. Given the importance of liquid water for terrestrial life, the liquid-water temperature interval is the commonly adopted definition, and a pressure-dependent, liquid-water habitability index (V13) can be defined. But also biological temperature-based considerations can provide further HZ definitions and can be all computed for each set of parameter choices (e.g. Silva et al. 2017a; Vladilo & Hassanali 2018). These more restrictive definitions, as compared to the liquid water index, may help to increase the probability of selecting surface ambient conditions that maximize the production and detectability of atmospheric biosignatures (a discussion on the necessity and possibly of the non-limiting assumption on searching for terrestrial-like life requirements can be found in e.g. McKay 2014; Kasting et al. 2014).

In this paper, we present a new release of the ESTM model, which we call EOS-ESTM. EOS is our new procedure for calculating RT in rocky planetary atmospheres with any pressure, chemical composition, and stellar spectral type (Simonetti et al. 2022). In our previous version we were limited to Earth-like systems. We have introduced and improved on several new parametrizations with respect to the V15 model, in particular for the treatment of the temperature dependence of the ice coverage over land and ocean, and for the zenith distance dependence of the surface albedo specifically for any type of surface. We have carefully calibrated EOS-ESTM to reproduce the Earth climate by making use of large recent satellite (CERES-EBAF Ed4.1; Loeb et al. 2018) and reanalysis (ERA5; Hersbach et al. 2020) data sets, and validated the predictive power of the model through detailed comparison with 1D and 3D models under a large range of physical conditions. We also provide a first exploration of the dependence of the maximum greenhouse distance of the HZ on planetary parameters, as compared to 1D-based values.

The paper is structured as follows. In Section 2, after a schematic summary of the ESTM model and parameters by V15, we provide a detailed description of each physical input of the model that has been either newly introduced or improved in the new EOS-

---

[14]The library of climate models used for this work was extracted from the ESTM-generated ARchive of TErrestrial-type Climate Simulations (ARTECS) available at https://wwwuser.oats.inaf.it/exobio/climates/ (Murante er al., 2020) . The data base is in continuous expansion.

ESTM release. In Section 3, we exploit the large amount and good quality of experimental data of the Earth climate system to calibrate and validate our Earth's model, the reference for habitable rocky exoplanets. In Section 4, we present the validation of EOS-ESTM for a large range of non-terrestrial conditions with a comprehensive comparison of the predictive power of our model with several other 1D and 3D models. Our summary and conclusions are finally presented in Section 5.

2 THE CLIMATE MODEL

In accordance with classic EBMs, the planetary surface is divided in a number N of latitude zones and the zonal surface quantities of interest are averaged over one rotation period. In this way, the surface quantities depend on a single spatial coordinate, the latitude ϕ. The thermal state of the surface is described by the temperature $T = T(t, \phi)$. Since the zonal quantities are averaged over one rotation period, the time t represents the seasonal evolution induced by the orbital eccentricity and tilt of the rotation axis. By assuming that the heating and cooling rates normalized per unit area are balanced in each zone, one obtains a set of N zonal energy balance equations

$$C \frac{\partial T}{\partial t} - \frac{\partial}{\partial x}\left[D\left(1-x^2\right)\frac{\partial T}{\partial x}\right] + I = S\left(1-A\right), \quad (1)$$

where we omit the index that runs from 1 to N for simplicity. The meaning of the terms in this equation can be summarized as follows.

(i) The term C represents the zonal heat storage and is expressed as heat capacity per unit area (J m^{-2} K^{-1}). It is calculated by summing the contributions of lands, C_l, oceans, C_o, ice over lands, C_{il}, and ice over oceans, C_{io}. These contributions are weighted according to the zonal coverage of each surface component.

(ii) The second term of equation (1) describes the meridional energy transport along the coordinate $x = \sin\phi$. The transport is modelled using the formalism of heat diffusion modulated by the parameter D (the diffusion term). As a major improvement with respect to classic EBMs, D is expressed as a function of the physical quantities that most affect the meridional transport, such as the planetary radius, rotational angular velocity, surface gravity, and surface atmospheric pressure. A detailed description of the physics behind this formalism can be found in V15.

(iii) The term I is the outgoing longwave radiation (OLR), which peaks in the thermal IR band for typical conditions of habitable planets. At variance with classic EBMs, I is estimated using single-column, radiative-convective calculations. By including the physics of the vertical transport, the ESTM becomes a 2D climate model, one dimension sampling the surface as a function of latitude, as in classic EBMs, the other dimension sampling the atmosphere as a function of height from the surface. In practice, we calculate I as a function of T for a given chemical composition and vertical stratification of the atmosphere. Compared to the original ESTM, the calculations of atmospheric radiative transfer that we present here have been greatly improved (see Section 2.6.1).

(iv) On the right hand of the equation (1), the term S represents the insolation, i.e. the incoming stellar radiation with maximum emission in the visible/near-IR spectral range. More specifically, the zonal, instantaneous stellar radiation that heats the planet, $S = S(t, \phi)$, is calculated taking into account the stellar luminosity, the orbital parameters and the inclination of the planet rotation axis. Details on these calculations can be found in V13.

(v) The term A is the albedo at the top of the atmosphere, i.e. the fraction of incoming photons that are reflected back in space without

Table 1. Treatment of the terms in equation (1) in classic EBMs, ESTM, and EOS-ESTM.

Term	Description	Classic EBMs	ESTM	EOS-ESTM	Reference to the most updated prescription
C	Thermal capacity	C = constant	Ocean, land, ice	ESTM + transient ice	This paper
D	Meridional transport	D = constant	$D = D(p, g, R_p, RH, \Omega_{rot})$	$D = D(p, g, R_p, RH, \Omega_{rot})$	Vladilo et al. (2015)
I	Outgoing longwave radiation	$I = I(T)$	CCM3 atmospheric RT	EOS atmospheric RT	Simonetti et al. (2022)
S	Insolation	$S = S(t, \phi)$	$S = S(t, \phi)$	$S = S(t, \phi)$	Vladilo et al. (2013)
A	Top-of-atmosphere albedo	$A = A(T)$	Surface & clouds +CCM3 atm. RT	Surface & clouds + EOS atm. RT	This paper; Simonetti et al. (2022)

Table 2. Main differences between ESTM and EOS-ESTM.

Model prescription	ESTM	EOS-ESTM	Reference in this paper
Stellar spectrum	Solar	Any spectral type	Section 2.6.1
Atmospheric composition	Earth-like	Variable bulk composition	Section 2.6.1
Greenhouse gases	Trace amounts of CO_2 and CH_4	Significant amounts of any greenhouse gas	Section 2.6.1
Surface albedo versus Z	Oceans	Oceans, lands, ice	Sections 2.1, 2.2, 2.3
Calibration of ice coverage	Based on Williams & Kasting (1997)	Based on Earth's satellite data	Section 2.3
Albedo and thermal inertia of transient ice	Not treated	Function of zonal ice cover	Section 2.4
Calibration of cloud albedo versus Z	Based on Cess (1976)	Based on CERES-EBAF satellite data	Section 2.5.2
Cloud short-wavelength transmission	Not treated	Two-valued function of T	Section 2.5.2
Cloud OLR forcing	Constant	Two-valued function of T	Section 2.5.3
Cloud coverage over ice	Constant	Decreasing with global ice coverage	Section 2.5.1

heating the planet. The calculation of A is extremely more detailed than in classic EBMs and is performed in several steps. First, we calculate the surface albedo, a_s, by weighting the albedo contribution of lands, a_l, oceans, a_o, ice on lands, a_{il}, and ice on oceans, a_{io}, according the respective fractional coverage. Then, the total albedo at the bottom of the atmosphere is calculated by summing the albedo of the clear-sky surface with the albedo of the clouds, weighted according to the fractional coverage of clouds. As an upgrade over the original EOS-ESTM, we now calculate the cloud albedo taking into account the reflection of the underlying surface (Section 2.5.2). Finally, the top-of-atmosphere albedo is calculated as a function of T, a_s and stellar zenith distance, Z, for a given chemical composition and vertical stratification of the atmosphere. These calculations are performed with the upgraded recipes of radiative transfer that we present here (Section 2.6.1). All the albedo prescriptions are calculated as a function of the zonal, instantaneous stellar zenith distance, $Z = Z(t, \phi)$. In the original, ESTM the albedo dependence on Z was considered for oceans, clouds, and atmosphere. Here, we improve formulas and we introduce this dependence also for lands and ice.

In Table 1, we summarize how the terms in equation (1) have been upgraded from classic EBMs to the ESTM. The main differences between the ESTM and the EOS-ESTM are summarized in Table 2. In the rest of this section, we review the prescriptions that we adopt to model the different components of the climate system, introducing the recipes that have been upgraded in the current EOS-ESTM version. Technical details on the solution of equation (1) in the course of the climate simulation can be found in V15 (Appendix A). In the present version of the code, we adopt 60 latitude zones, a starting temperature of $T_0 = 300$ K, and a tighter criterion of convergence for the global mean temperature, $\langle T \rangle$: in practice, after running 20

orbits, the convergence is considered to be achieved when $|\delta \langle T \rangle / \langle T \rangle|$ < 10^{-5} in two consecutive orbits. All these parameters can be changed according to specific needs. For instance, T_0 can be varied in studies of climate bistability where two stable solutions (a Snowball state and a warm state) can be found in an appropriate parameter range depending on the initial temperature. As in most EBMs, the original ESTM Murante et al. (2020) and EOS-ESTM produce climate bistability.

2.1 Oceans

2.1.1 Ocean fraction

The coverage of oceans on the planetary surface is parametrized by assigning a fractional area coverage of oceans, f_o, to each latitude zone. This parametrization is sufficient to test the climate impact of different latitudinal distributions and oceans, including the extreme cases of ocean worlds ($f_o = 1$ in each zone). Oceans are characterized by their specific properties of albedo and thermal inertia.

2.1.2 Ocean albedo

The surface reflectivity of the oceans is modelled using empirical laws that take into account its dependence on Z and the fact that the water surface is not smooth. We compared previous algorithms published in the literature (Briegleb et al. 1986; Enomoto 2007) with a recent set of measurements obtained at different values of Z (Huang et al. 2019). The observational data (red dots in Fig. 1) show a large spread at any value of Z due to the variations of atmospheric transmittance created by scattering and absorption of sunlight in the atmosphere (Payne 1972). To model the ocean albedo we are interested in the data in clear sky conditions, since the
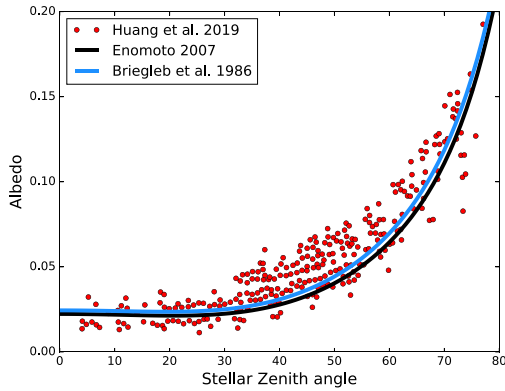
Figure 1. The albedo of oceans as a function of the stellar zenith angle, Z. The blue and black lines represent the formulation adopted in Briegleb et al. (1986) and Enomoto (2007), respectively. Red dots represent the data obtained from Huang et al. (2019, fig. 5a).

transmittance of the atmosphere is accounted for in our radiative transfer calculations (Section 2.6.1). The lower envelope of the data in Fig. 1 represents the clear-sky case. The formula proposed by Enomoto (2007) (black line) and Briegleb et al. (1986) (blue line) are also shown in the figure. One can see that the expression proposed by Enomoto (2007), namely

$$a_o = \frac{0.026}{1.1\mu^{1.7} + 0.065} + 0.15(\mu - 0.1)(\mu - 0.5)(\mu - 1.0) , \qquad (2)$$

(where $\mu = \cos Z$) yields a slightly better match to the lower envelope of the data. We therefore adopt this expression as in V15. We do not propose an expression to match the lowest points of the observational data set because we do not have information about the measurement errors and we cannot exclude the presence of outliers.

Despite having being calibrated with the Earth's oceans, the empirical law (2) can be reasonably applied to any exoplanetary ocean, since the zenith dependence basically follows the universal Fresnel formula (WK97), corrected for the roughness of the surface.

2.1.3 Thermal inertia of oceans

Due to the high thermal capacity of water, the thermal inertia of oceans, C_o, gives a major contribution to the term C. The full oceanic contribution, which is effective over long time scales (typically decades on Earth), is not treated in the ESTM. However, the short-term thermal impact of the oceans is accounted for by considering the contribution of the mixed layer, i.e. the surface layer of water that exchanges heat with the overlying atmosphere (Pierrehumbert 2010, hereafter P10). In the original version of ESTM, we adopted a mixed-layer contribution $C_{ml} = C_{ml50}$ (WK97,P10), corresponding to thermal inertia of a 50-m, wind-mixed ocean layer (see Table 3). In Section 3, we present a new tuning of this parameter based on the short-term monthly variations of Earth's surface temperatures. For exoplanets with shallow oceans, C_{ml} can be changed to simulate the impact of water layers of different depths.

2.2 Lands

2.2.1 Land fraction

The surface fraction of continents is described by assigning a fractional area of land $f_l = 1 - f_o$, to each latitude zone. This

parametrization is sufficient to test the climate impact of extreme distributions of continents, such as polar or equatorial continents, or desert worlds ($f_o = 0$ in each zone). Continents are characterized by their specific properties of albedo and thermal inertia.

2.2.2 Land albedo

To model the albedo of land, we adopt a formulation proposed by Briegleb (1992), namely

$$a_x(\mu) = a_x(0.5)\frac{1 + d}{1 + 2 d \mu} \qquad (3)$$

where $a_x(0.5)$ is the albedo of a surface x when $\mu = 0.5$ ($Z = 60°$), and the parameter d regulates the dependence on stellar zenith distance ($d = 0.1$ for a 'weak' dependence; $d = 0.4$ for a 'strong' dependence). These parameters can be varied according to the type of surface (desert, basalt, vegetation, etc.) in order to model planets with specific characteristics (Coakley 2003, table 3 therein). The adopted values should be representative of clear-sky conditions, since ESTM takes into account the effects of the atmospheric albedo separately (Section 2.6.1).

2.2.3 Thermal inertia

The solid surface has a negligible thermal capacity compared to that of the oceans and even compared to that of a relatively thin, Earth-like atmosphere. The value of land thermal inertia that we adopt (Table 3) is representative of a layer of rock with thickness of 0.5 m (Vladilo et al. 2013). Even if small, this value becomes important in planets without oceans and with extremely thin atmospheres.

2.3 Ice

2.3.1 Ice fraction

ESTM calculates the fractional coverage of ice over lands, f_{il}, and oceans, f_{io}, making use of temperature-dependent algorithms. These prescriptions are critical because the ice coverage plays a key role in the albedo-temperature feedback and affects the lower temperature limit of liquid-water habitability. We paid special attention to recalibrate the algorithms by searching for (i) a new set of experimental data and (ii) an appropriate functional dependence on T.

(i) The distribution of ice on the Earth surface was derived from measurements obtained from NASA's Terra and Aqua satellites[15] in the period 2005–2015. To find a trend with temperature, we associated the mean annual temperature of each latitude zone to the corresponding fraction of ice. The temperature data were obtained from the ERA5 data set[16] (Hersbach et al. 2020) in the same period. This exercise was done separately for ice on lands and on oceans. To minimize the impact of orographic/oceanographic conditions specific of the Earth, we considered only land data in areas unaffected by local mountains and altitude below the freezing level and we excluded ocean data at the edge of Antarctica.[17] The results are

---

[15]See https://modis.gsfc.nasa.gov/
[16]See https://climate.copernicus.eu/climate-reanalysis
[17]The combined effect of katabatic winds and ocean currents form mesoscale areas of open water near the Antarctica coastline, known as polynyas (Stringer & Groves 1991). These areas fringe the edge of the continent owing to the opening waterways (known as flaw leads) produced by the interconnection between themselves (Meredith & Brandon 2017).

Table 3. Adopted terms for thermal inertia.

Parameter	Description	Adopted value	Comments
C_{ml50}	Thermal inertia of the water mixed layer	210×10^6 J m^{-2} K^{-1}	Equivalent to a 50-m water layer (Pierrehumbert 2010)
$C_{atm, \circ}$	Thermal inertia of the atmosphere	10.1×10^6 J m^{-2} K^{-1}	Equivalent to a 2.4-m water layer (Pierrehumbert 2010)
C_{solid}	Thermal inertia of the solid surface	1×10^6 J m^{-2} K^{-1}	Equivalent to a 0.5-m rock layer (Vladilo et al. 2013)

shown in Fig. 2, where the data (filled and empty circles) show that the dependence on T is quite different for lands and oceans (green and blue colours, respectively). The empirical trends show two features: (1) a very sharp rise of ice coverage below the water freezing point and (2) the existence of a small fraction of ice coverage at T slightly above the freezing point. The exponential model adopted in WK97 and in previous versions of the ESTM (dashed line in the left-hand panel) is not able to reproduce these two features, indicating the need of a new type of functional dependence.

(ii) After trying different types of functions, we found that the empirical trends of Fig. 2 can be well approximated using a generalized logistic function (Richard 1959). Based on the physical boundary conditions of our problem, we chose a function that vanishes at very high T and tends to 1 at very low T:

$$f_{ix}(\overline{T}) = \frac{1}{\left[1 + \xi_x \, e^{\theta_x (\overline{T} - T_{\circ,x})} \right]^{1/\xi_x}} \tag{4}$$

where $\overline{T}$ is the zonal temperature averaged over a time τ_{ice} representative of the time-scale of ice growth/melting; the index x refers to the type of surface underlying the ice cover ($x = o$ for oceans and $x = l$ for lands); $T_{\circ}$ is the temperature turning point for the liquid-solid transition of water; θ is the growth rate; and ξ is the shape parameter. The zonal temperature $\overline{T}$ is averaged over the interval τ_{ice} that precedes the current time of the climate simulation. For consistency with the data shown in Fig. 2, which have been averaged over 1 year, we adopt $\tau_{ice} = 12$ months. The parameters $T_{\circ}$, θ, and ξ were tuned using: (i) the data versus temperature shown in the right-hand panel of Fig. 2, and (ii) the data versus latitude of the Earth's reference model (bottom right panel in Fig. 8). The adopted parameter values are listed in Table 4. The resulting logistic functions (solid curves in the right-hand panel of Fig. 2) are able to reproduce the observed sharp rise below the turning point $T_{\circ}$ and the existence of a small ice fraction slightly above $T_{\circ}$.

2.3.2 Albedo of frozen surfaces

The albedo of frozen surfaces (ice and snow) shows a remarkable scatter in Earth measurements, with temporal variations that take place on different time-scales. In ESTM, we adopt representative values based on average conditions. As an upgrade with respect to the previous version, we model the albedo of ice with equation (3). For stable ice on lands and oceans we adopt $a_{il}(0.5) = 0.70$ $a_{io}(0.5)$ = 0.55, respectively. In both cases we set $d = 0.1$, i.e. a 'weak' dependence on μ (Briegleb 1992). These values provide a good match to Earth's zonal albedo (Section 3), but can be changed to model exoplanets with specific properties of frozen surfaces.

2.3.3 Thermal inertia

The contribution to thermal inertia of ice is important only if the planet lacks oceans and has an extremely thin atmosphere. For icy surfaces, we adopt the same representative value adopted for any solid surface (Table 3). For icy surfaces over oceans, following WK97, we

add a small contribution (10.5×10^6 J m^{-2} K^{-1}) representative of the thermal inertia of the underlying water.

2.4 Transient ice

The albedo and thermal capacity of transient ice (ice that is forming or melting) are different from those of stable ice. A possible way to take into account this effect is to introduce specific ice parameters in a temperature range around the water freezing point (WK97). However, this approach requires the introduction of several parameters not easy to quantify (the albedo and thermal capacity of unstable ice and the temperature range where the transition takes place). To avoid this additional parametrization, we adopt a prescription that provides a gradual change of the albedo and thermal capacity from the case in which the ice is totally absent, to the case in which the ice is stable.

2.4.1 Albedo of transient ice

The albedo of stable ice over lands, $a_{il, s}$, and of stable ice over oceans, $a_{io, s}$, is higher than the albedo of the underlying surface. When the temperature increases and the ice becomes more and more patchy, the albedo of unstable ice gets closer and closer to the albedo of the underlying surface. To simulate this transition, we assume that the fractional coverage of ice (4) is a reasonable estimator of the patchiness of the ice and we adopt the expressions

$$a_{il}(\overline{T}) = a_l + (a_{il,s} - a_l) \, f_{il}(\overline{T}) \tag{5}$$

for ice over lands and

$$a_{io}(\overline{T}) = a_o + (a_{io,s} - a_o) \, f_{io}(\overline{T}) \tag{6}$$

for ice over oceans. In this way, the albedo attains the high values typical of stable ice only when the ice coverage is complete. When the ice coverage is absent, the albedo equals that of lands (a_l) or oceans (a_o) without ice. The parameters in the above equations are calculated for $\mu = 0.5$ (see Table 7) and the albedo dependence on μ is modelled as explained in Section 2.3.2.

2.4.2 Thermal inertia of transient ice

For the thermal inertia of transient ice, we follow the same approach used for the albedo of transient ice. For the oceans, which provide the main contribution to the thermal inertia, we adopt the relation

$$C_{io}(\overline{T}) = C_o + (C_{io,s} - C_o) \, f_{io}(\overline{T}) \, , \tag{7}$$

where $C_{io, s}$ is the thermal inertia of stable ice over ocean. For land, the contribution is very small, and there is no need to adopt a similar relation since in our parametrization $C_{il, s} = C_l$.

2.5 Clouds

The complexity of the physics of cloud formation and the lack of fluidodynamics and 3D capabilities of ESTM prevent us to model
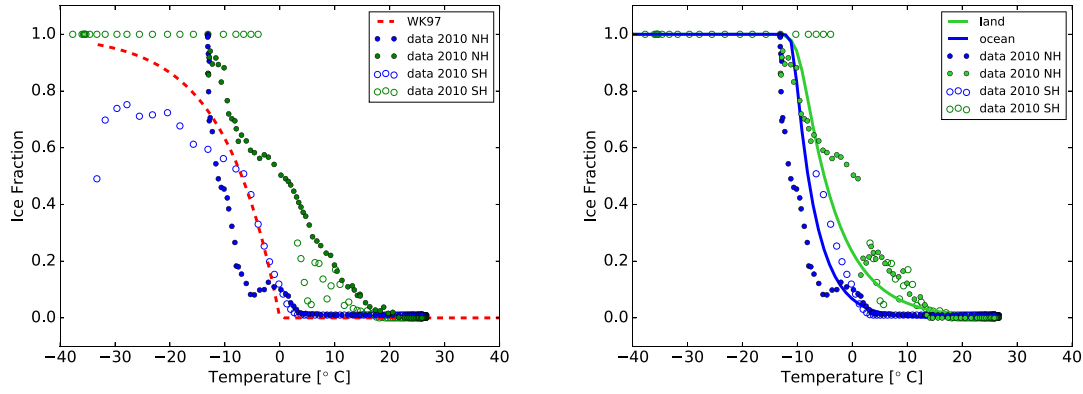
Figure 2. Mean-annual values of Earth's ice cover over lands and oceans plotted as a function of the mean annual zonal surface temperature. Left-hand panel: Observational data for lands (green symbols) and oceans (blue symbols) obtained with ERA5 reanalysis and NASA's Terra and Aqua Satellites averaged over the 2010; filled and empty circles represent data collected from the Northern and Southern hemisphere, respectively; red dotted line: prescription for the ice cover adopted in previous versions of ESTM. Right-hand panel: same as in the left-hand panel, but excluding data with altitude above the freezing level and the ocean data at the edge of Antarctica; solid lines: prescriptions adopted in this work for lands (green line) and oceans (blue line); land data influenced by local orographic conditions specific of the Earth have been ignored; see Section 2.3.1.

Table 4. Parameters adopted for the ice coverage function (4).

Parameter	Description	Value
Land		
$T_{\circ l}$	Temperature turning point	265.15 K
θ_l	Growth rate	1.2
ξ_l	Shape parameter	8.0
Ocean		
$T_{\circ o}$	Temperature turning point	263.15 K
θ_o	Growth rate	3.0
ξ_o	Shape parameter	12.0

the spatial distribution and physical properties of clouds in a self-consistent way. Clouds are treated as bottom-of-the atmosphere features with parametrized values of coverage, albedo, and OLR forcing. Given their critical role in the climate energy budget, we introduced upgraded algorithms for all these features.

2.5.1 Cloud fraction

The cloud fraction is estimated with the expression

$$f_c = f_o \left[(1 - f_{io}) f_{co} + f_{io} f_{ci} \right] + f_l \left[(1 - f_{il}) f_{cl} + f_{il} f_{ci} \right] \quad (8)$$

where f_{co}, f_{cl}, and f_{ci} are representative values of the cloud coverage over oceans, lands, and ice, respectively (see Table 5). These values are based on Earth data but, in principle, can be tuned for other planets. In the original version of ESTM a constant cloud coverage over ice is adopted. This approach is reasonable when ice is not dominant, as in the case of the present-day Earth. However, when the planet undergoes a transition to a snowball state, the global fraction of clouds is expected to decrease. To capture this effect, we introduce a parameter $f_{c, sb}$, representative of the cloud coverage in a snowball planet, and we adjust f_{ci} in the course of the climate simulation introducing a dependence on the globally averaged ice fraction, $\langle f_{ice} \rangle$. In practice, we adopt the expression

$$f_{ci} = \left(f_{ci, \oplus} - f_{c,sb} \right) \left(\frac{1 - \langle f_{ice} \rangle}{1 - \langle f_{ice} \rangle_\oplus} \right) + f_{c,sb} \quad , \quad (9)$$

where $f_{ci, \oplus}$ is the cloud coverage over ice calibrated with Earth's data. With this prescription, $f_{ci} = f_{c, sb}$ when the planet enters a hard

snowball state ($\langle f_{ice} \rangle = 1$). The parameter $f_{c, sb}$ can in principle be tuned from results of GCM simulations of snowball planets (Abbot 2014). The Earth model is not affected by the choice of $f_{c, sb}$ because $f_{ci} = f_{ci, \oplus}$ when $\langle f_{ice} \rangle = \langle f_{ice} \rangle_\oplus$.

2.5.2 Cloud albedo

To upgrade the prescriptions for the albedo of the clouds we: (i) used an updated set of Earth satellite data; (ii) adopted a new functional form for the dependence of the cloud albedo on μ; and (iii) introduced a dependence of the effective cloud albedo, a'_c, on the albedo of the underlying surface, a_s.

(i) To upgrade the experimental data, we use the recent set of top-of-atmosphere (TOA) albedo data obtained from the CERES-EBAF satellite (Loeb et al. 2018). Following equation (8) by Cess (1976), we estimate the zonal TOA albedo of the clouds with the expression

$$A_{c,obs} = \frac{A_{obs} - A_{obs,clear} (1 - f_c)}{f_c} , \quad (10)$$

where A_{obs} are the TOA albedo data obtained in a given zone, $A_{obs, clear}$, the TOA albedo data obtained in the same zone in clear-sky conditions, and f_c is the fractional cloud coverage in the latitude zone of interest. To extract the dependence on zenith distance, the derived values of $A_{c, obs}$ are associated with the mean annual value of $\mu = \cos Z$ of the zone of interest, $\overline{\mu}$. In Fig. 3, we compare the cloud albedo versus $\overline{\mu}$ that was obtained by Cess (1976) from the data set by Ellis & Haar (1976), with the results that we obtain inserting the CERES-EBAF data for the period 2005–2015 in equation (10). One can see that the use of the updated and extensive data set provided by CERES leads to significant differences. In particular, the cloud albedo becomes weaker in the equatorial regions. We use this updated data set to improve the description of the cloud albedo with respect to previous parametrizations (WK97, V15), which were based on Cess (1976).

(ii) In previous work, the dependence of the cloud albedo on the zenith distance was modelled using the linear form $a_c = \alpha + \beta Z$ (WK97, V13). To prevent the existence of negative values of albedo at low Z, V15 introduced a third parameter (the minimum value of cloud albedo at low zenith distances, $a_{c, min}$), and used the expression $a_c = \max \{ a_{c, min}, (\alpha + \beta Z) \}$. Here, for consistency with the description

Table 5. Astronomical and planetary Earth data.

Parameter	Description	Adopted value	Reference/Comments
$S_\circ$	Mean annual insolation	1361.0 W m^{-2}	CERES-EBAF (2005–2015)
e	Orbital eccentricity	0.01671022	
ϵ	Axis obliquity	23.43929	
g	Surface gravity acceleration	9.81 m s^{-2}	

Note.[a] Adopted Earth's values can be changed to model exoplanets with different types of stellar, orbital, and planetary properties.
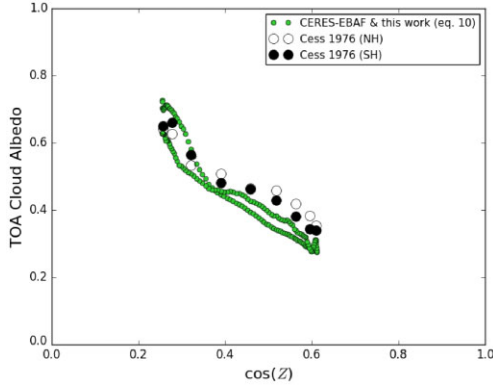
Figure 3. TOA cloud albedo profile obtained using the data collected from CERES-EBAF (green dots) in the period 2005–2015 compared with Cess (1976) data for the NH (empty circles) and SH (black circles). The albedo is plotted versus the mean-annual Solar zenith angle of each latitude zone.
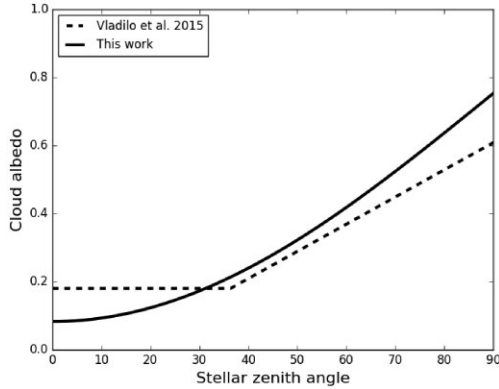
Figure 4. Comparison of the cloud albedo models adopted in V15 (dashed line) and in this work (solid line). See Section 2.5.2.

of the albedo of land, ice, and ocean, we adopt a dependence on μ, rather than on Z, also for the cloud albedo. In practice, we adopt

$$a_c(\mu) = a_c(0.5) + m_c \left(\mu - \frac{1}{2}\right) \qquad (11)$$

where m_c is the slope and $a_c(0.5)$ is the cloud albedo at $\mu = 0.5$. As can be seen in Fig. 4, this new function (solid line) yields positive values at low Z without the need of an extra parameter, and yields a smoother dependence on Z than the previous prescription (dashed line).

(iii) Polar clouds have a relatively high transmittance of short-wavelength photons, and part of the photons are reflected by the underlying surface, making their path up to the outer space through the clouds and the atmosphere. This effect becomes particularly

important when the underlying icy surface is very reflective. The impact of this effect can be appreciated in Fig. 3, where one can see that at low μ, in correspondence with the ice polar caps, the slope of the Earth's cloud albedo versus μ becomes steeper. To incorporate this effect in our model we follow Thompson & Barron (1981) and, based on their equation (A14), we calculate the effective cloud albedo over reflective surfaces,

$$a_c' = a_c + \frac{(1 - a_c)(1 - a_c^*)}{a_c^*} \times [(1 - t^2 a_s^* a_c^*)^{-1} - 1] \qquad (12)$$

where a_c is the cloud albedo over a non-reflective surface, a_c^* is the cloud albedo for diffuse radiation, a_s^* is the surface albedo for diffuse radiation; the values of diffuse albedo are estimated from the corresponding direct albedo calculated at $\mu = 0.5$; the parameter t is an estimator of the transmittance, i.e. the radiation fraction not absorbed between the cloud top and the surface. We model t with the function

$$t = 0.90 - 0.05 \tanh\left(\frac{T - 263.15\,\text{K}}{10\,\text{K}}\right) \qquad (13)$$

which provides a smooth transition between the typical transmittance of thin polar clouds ($t \simeq 0.95$; Thompson & Barron 1981) and the lower transmittance in regions without surface ice. In these regions, the surface albedo is low, the term $t^2 a_s^* a_c^*$ is small, and the exact choice of t has a modest impact on the calculation of a_c' with equation (12).

2.5.3 Cloud OLR forcing

In the original version of the ESTM, the cloud OLR forcing had a constant value. This approach is unsatisfactory since the OLR measurements of terrestrial clouds show an extremely large seasonal and latitudinal scatter (Hartmann, Ockert-Bell & Michelsen 1992, fig. 10 therein). As an attempt to introduce a variable value by capturing a dependence on T, we tried to scale the cloud OLR according to the water vapour content of the atmospheric column, which is a function of T at constant relative humidity. However, this attempt did not provide a good match to the experimental data. This is not too surprising, given the complexity of the physics of cloud formation and cloud radiative transfer, which depends on a variety of thermodynamical and microscopic factors not treated in our model. Despite the negative result of this attempt, we decided to take into account the properties of clouds over icy regions as an upgrade of our model. Terrestrial clouds over icy regions show a very small OLR forcing, typically one order of magnitude smaller than the average value (Hartmann et al. 1992, , fig. 10 therein). To capture this effect, we calculate the cloud OLR forcing (also called cloud radiative effect, *CRE*) with the following expression:

$$CRE = CRE_\circ \left[0.60 + 0.40 \tanh\left(\frac{T - 263.15\,\text{K}}{10\,\text{K}}\right)\right] \qquad (14)$$

where $CRE_\circ$ is a representative value that can be calibrated with terrestrial clouds (see Section 3.1.2) and the term in square brackets varies smoothly from 1, at high T, to 0.2, at very low T. The above expression provides a smooth transition with decreasing T that mirrors the increase of cloud transmittance adopted in equation (13). This simplified formalism is justified by the fact that it improves the match between predicted and observed zonal OLR in the Northern polar regions (see Section 3).

2.6 Atmosphere and top of atmosphere

2.6.1 Clear-sky radiative transfer

The vertical radiative transport of energy throughout the atmosphere has a strong impact on the I and A terms in equation (1) and therefore plays a central role in the climate simulations. In the previous version of ESTM, the terms I and A were estimated using the radiative transfer model developed as part of the Community Climate Model 3 (CCM3; Kiehl et al. 1998), which is based on the HITRAN 1992 spectroscopic repository data (Rothman et al. 1992). CCM3 is a band model tailored for an Earth-like atmosphere illuminated by solar-type radiation. As such, the concentrations of greenhouse gases can only be varied in trace abundances, the list of greenhouse gases cannot be expanded, and it is not possible to model stellar spectra different from the solar one. To overcome these limitations and to use an updated repository of spectroscopic data, the new version of ESTM uses the EOS radiative transfer procedure (Simonetti et al. 2022) to calculate the terms I and A.

EOS is a line-by-line procedure based on the publicly available opacity calculator HELIOS-K (Grimm & Heng 2015; Grimm et al. 2021) and the radiative transfer code HELIOS (Malik et al. 2017, 2019). Line absorption from N_2, O_2, H_2O, CO_2, and CH_4 are calculated using data from the HITRAN 2016 (Gordon et al. 2017) repository. The continuum of H_2O is included via the standalone version of the CNTNM routine of the LBLRTM code (Clough et al. 2005), which runs the MT_CKD v3.4 opacity model (Mlawer et al. 2012). For CO_2-dominated atmospheres, the collision-induced absorption (CIA) and the sub-Lorentzian absortion lines shape of CO_2 are also taken into account and calculated from, respectively, HITRAN data and the recipes in Perrin & Hartmann (1989). The EOS model has the advantage of not being tied to a specific type of atmosphere via e.g. gas opacity parametrizations, thus allowing a far greater flexibility in choosing the composition of the atmosphere. Radiative transfer calculations are performed on a 60-layer atmospheric column logarithmically spaced in pressure, from the ∼1 bar surface to the 1 μbar TOA level (10 layers per order of magnitude). The OLR is evaluated as a function of T every 20 K below 280 K, every 10 K between 280 and 310 K and every 5 K up to 360 K. The TOA albedo is evaluated every 20 K in the entire T range up to 360 K, for $Z \in$ (0°, 30°, 45°, 60°, 70°, 75°, 80°, 83°, 85°, 87°, 88°, 89°) and for $a_x \in$ (0.0, 0.15, 0.30, 0.60, 0.90). We adopted a non-equally spaced grid in order to sample more precisely the regions in which the OLR and the TOA albedo change their slopes. Multilinear interpolation on both OLR and TOA albedo tables is then carried out by ESTM. Thanks to the fact that HELIOS and HELIOS-K run on GPU processors (also known as graphic cards or accelerators) it is possible to calculate the line-by-line radiative transfer in a reasonable amount time even on desktop machines. As reported in Grimm et al. (2021), GPU-based codes can be more than an order of magnitude faster than CPU-based ones. Starting from the HITRAN line parameters files, EOS requires ∼70 h to calculate the OLR and TOA albedo tables for a specific

atmosphere.[18] Thanks to the modularity of the EOS procedure, part of the results obtained in the early steps can be reused, reducing the total time for the calculations of new cases.

2.6.2 Top-of-atmosphere albedo

The top-of-atmosphere (TOA) albedo is tabulated as a function of T for a given set of atmospheric parameters, using radiative transfer calculations in the short wavelength (visible, near-IR) spectral range. Since the TOA albedo also depends on the surface albedo, a_s, and the stellar zenith distance, Z, the calculations of the TOA albedo must sample the parameter space (T, a_s, Z). The wavelength dependence of the short wavelength scattering implies that the albedo is sensitive to the spectral distribution of the host star. The new radiative transfer procedure that we adopt allows us to tabulate A for planetary atmospheres illuminated by stars of different spectral type.

2.6.3 OLR

For a given set of atmospheric parameters (surface gravity, surface pressure, chemical composition, relative humidity, vertical structure), the OLR in the thermal IR band is computed as a function of surface temperature T by using a reverse calculation of radiative transfer where the temperature of the lowest atmospheric layer is forced to be equal to T. The resulting OLR tables, calculated in clear-sky conditions, are given in input to the climate simulation. The OLR forcing of clouds calculated with equation (14) is then subtracted from the clear-sky OLR.

2.6.4 Thermal inertia of the atmosphere

The atmospheric thermal inertia is much smaller than the oceanic one and can be neglected in planets with oceans and thin, Earth-like atmospheres. However, in general, the atmospheric thermal inertia must be taken into account, since habitable planets may lack oceans and/or may have thick atmospheres. For this reason, in our formulation we scale the thermal inertia of the Earth's atmosphere (Table 3) according to the thermal capacity and columnar mass of the planetary atmosphere (V15). The thermal capacity is calculated for the specific atmospheric composition; assuming hydrostatic equilibrium, the atmospheric columnar mass is calculated as p/g, where p is the surface atmospheric pressure and g is the surface gravitational acceleration. The atmospheric contribution to thermal inertia is summed to the ocean, land, and ice contributions described above.

3 THE REFERENCE EARTH MODEL

In this section, we present the calibration and the validation tests of the model applied to Earth, which represents the reference for modelling habitable exoplanets of terrestrial type. The large amount and good quality of experimental data of the Earth climate system provide the best way for adjusting many important model parameters

---

[18]Estimates obtained using a workstation equipped with an nVidia RTX 2080 graphic card, a 7200 rpm HP/Seagate hard drive and an Intel Xeon Silver 4108 CPU. The reading-writing times from the storage memory (hard drive or solid state memory) and the CPU efficiency play important roles in determining the final amount of time required by the procedure, which can be consistently different on other machines.

Table 6. Earth satellite data and results of the Earth reference model.

Quantity	Description	Earth value	Model	Units
$\langle T \rangle$	Global surface temperature	287.5^a	288.7	K
$\langle T \rangle_{NH}$	Mean surface temperature of Northern hemisphere	288.4^a	288.5	K
ΔT_{PE}	North Pole–Equator temperature difference	38.9^a	41.1	K
$\langle h \rangle_{NH}$	Fraction of habitable surface (Northern hemisphere)	0.866^b	0.855	...
$\langle A \rangle$	Global top-of-atmosphere albedo	0.314^c	0.315	...
$\langle A \rangle_{NH}$	Mean top-of-atmosphere albedo of Northern hemisphere	0.310^c	0.314	...
$\langle OLR \rangle$	Global outgoing longwave radiation	240.2^c	241.4	W m^{-2}
$\langle OLR \rangle_{NH}$	Mean outgoing longwave radiation of Northern hemisphere	240.8^c	241.6	W m^{-2}
$\langle f \rangle_c$	Global cloud fraction	0.674^c	0.666	..
$\langle f \rangle_{c,\,NH}$	Mean cloud fraction of Northern hemisphere	0.644^c	0.646	..
Φ_{max}	Peak of atmospheric transport at mid latitudes	5.0^d	5.0	PW

Notes. [a] Average ERA5 temperatures in the period 2005–2015.
[b] Average fraction of planet surface with temperature satisfying the liquid water criterion.
[c] Average CERES-EBAF data in the period 2005–2015.
[d] Trenberth & Caron (2001).

and testing the new recipes that we have introduced in the previous section.

3.1 Astronomical and planetary quantities

The values of astronomical and planetary quantities that we adopt for the reference Earth model are listed in Table 5. Global values of planetary temperature, OLR, and albedo taken from satellite observations (CERES-EBAF and ERA5) are summarized in Table 6. Unless differently specified, all data were averaged for the period 2005–2015. For consistency, the insolation S and the volumetric mixing ratio of CO_2 and CH_4 were estimated for the same time period. For the solar constant, we adopt $S_0 = 1361$ W m^{-2} in accordance with the mean annual insolation value measured from CERES-EBAF (1361.16 W m^{-2}).

3.1.1 Surface albedo

The adopted values of albedo are listed in Table 7. For the albedo of lands, we adopt a value representative of the Earth continents, namely $a_l(0.5) = 0.20$, which is an intermediate value between bare and vegetation-covered soil. As far as the dependence with μ is concerned, we adopt a 'weak' dependence ($d = 0.1$), which is representative of most types of Earth's continental surfaces (Briegleb 1992; Coakley 2003).

3.1.2 Clouds

The parameters adopted for the clouds fraction on land, ocean, and ice are shown in Table 7. With respect to V15, the coverage over land and ocean, f_{cl}, f_{co}, were updated following the experimental data by King et al. (2013), while the adopted value of coverage over ice, f_{ci}, was estimated from the CERES-EBAF satellite data.

Table 7. Parameters of surface and cloud albedo.

Parameter	Description	Adopted value	Comments
a_l	Albedo of lands (at $\mu = 0.5$)	0.20	Tuned to match zonal albedo profile (Fig. 8)
$a_{il,s}$	Albedo of stable frozen surfaces (at $\mu = 0.5$)	0.70	Tuned to match zonal albedo profile (Fig. 8)
$a_{io,s}$	Albedo of stable ice on ocean (at $\mu = 0.5$)	0.55	Tuned to match zonal albedo profile (Fig. 8)
a_c	Albedo of clouds (at $\mu = 0.5$)	0.44	Tuned to match CERES-EBAF data (Fig. 6)
m_c	Slope of cloud albedo equation	-0.67	Tuned to match CERES-EBAF data (Fig. 6)
f_{cw}	Cloud coverage on water	0.72	King et al. (2013)
f_{cl}	Cloud coverage on land	0.55	King et al. (2013)
f_{ci}	Cloud coverage on ice	0.56	Tuned to match the cloud coverage of Earth's North Hemisphere

Table 8. Atmospheric radiative transfer parameters for the Earth's reference model.

Quantity	Description	Adopted value	Reference/comments
p_{dry}	Surface pressure dry air	10^5 Pa	
r	Relative humidity	60 per cent	Vladilo et al. (2015)
c_{CO2}	Atmospheric concentration of CO_2	350 ppm	See section 3.1.3
c_{CH4}	Atmospheric concentration of CH_4	1.7 ppm	See section 3.1.3
T_{tp}	Temperature of tropopause	200 K	Seidel et al. (2001), Kuell et al. (2005)
$CRE_\circ$	TOA longwave forcing of clouds	26.1 W m^{-2}	tuned to match the OLR profiles in Figs 7 and 8

The value of the cloud radiative forcing for longwave radiation, which acts as a parameter in the model, was tuned in order to obtain a better match in the OLR profiles in Figs 7 and 8. By adopting $CRE_\circ = 26.1$ W m^{-2} in equation (14), we obtain an average value $\langle CRE_{olr} \rangle = 25.5$ W m^{-2} for the Earth model. This is in excellent agreement with the mean value of the Earth, 25.8 W m^{-2}, obtained from CERES-EBAF Ed4.1, also considering the still large uncertainty on this quantity found in the literature.

3.1.3 Atmospheric quantities

Table 8 shows the atmospheric quantities adopted in the EOS radiative transfer calculations of the Earth model. Following Seidel et al. (2001) and Kuell et al. (2005), we adopt a temperature for the tropopause $T_{tp} = 200$ K. We adopt a relative humidity of 60 per cent, in agreement with the global relative humidity measured on Earth, a surface pressure of dry air of $p_{dry} = 1.00 \times 10^5$ Pa and a volumetric concentration for CH_4 of 1.7 ppmv. The CO_2 gas concentration of the reference period 2005–2015 ($c = 390$ ppm, derived from the NOAA data base[19]) has been corrected to compensate the net TOA radiative imbalance of $\Delta F \simeq 0.6$ W m^{-2} (Wild et al. 2013) observed in

[19]https://gml.noaa.gov/ccgg/trends/

Table 9. Parameters for the meridional transport.

Quantity	Description	Adopted value	Reference/comments
$D_\circ$	Coefficient of latitudinal transport	0.66 W m^{-2} K^{-1}	Tuned[a] to match the zonal temperature profile (Fig. 8)
R	Modulation of latitudinal transport	1.4	Tuned to match the zonal temperature profile (Fig. 8)
$\Lambda_\circ$	Ratio of moist over dry eddie transport	0.7	V15; fig. 2 in Kaspi & Showman (2015)

Note.[a] $D_\circ$ is also tuned to match the Earth's peak of atmospheric transport at mid latitudes, Φ_{max} (Table 6).
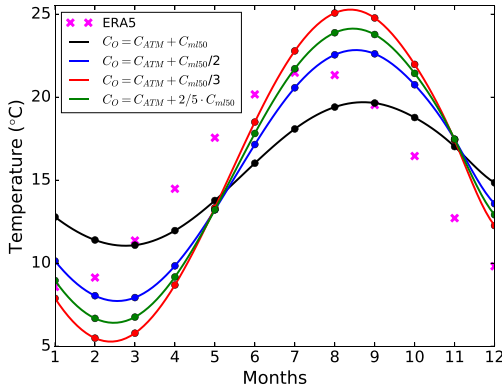
Figure 5. Seasonal evolution of mean surface temperature as a function of the effective thermal capacity. The black, blue, green, and red lines represent the thermal capacities of oceans C_o with $C_{ml50} = 210, 105, 70$, and 84×10^6 J m^{-2} K^{-1}, respectively. Magenta crosses: averaged ERA5 temperatures in the period 2005–2015 for the North Hemisphere (NH).

the current transient climate, since we will be performing constant-forcing simulations. We used the simplified analytical expression linking CO_2 concentration changes to the resulting radiative forcing change (Myhre et al. 1998):

$$\Delta F = \alpha \ln\left(\frac{c}{c_0}\right) \quad (15)$$

with $\alpha = 5.35$ W m^{-2}, leading to a corrected volumetric mixing ratio for CO_2 of $c_0 = 350$ ppm.

3.1.4 Meridional transport

The parameters adopted for the meridional transport are shown in Table 9. The parameter $D_\circ$ was tuned to match the Earth's peak of atmospheric transport at mid-latitudes, Φ_{max} (5.0 PW; Trenberth & Caron 2001) and the temperature-latitude profile in Fig. 8. We refer to V15 for a full description of the parameters listed in the table.

3.1.5 Depth of the mixed ocean layer

To tune the mixed ocean layer parameter, C_{ml}, we investigated the monthly excursions of the Earth global surface temperature. In Fig. 5, we compare the annual evolution of this quantity observed in the Northern hemisphere (crosses) with the predictions of our model obtained for different choices of C_{ml} (solid lines). One can see that by increasing C_{ml}, the maximum annual excursion of monthly surface
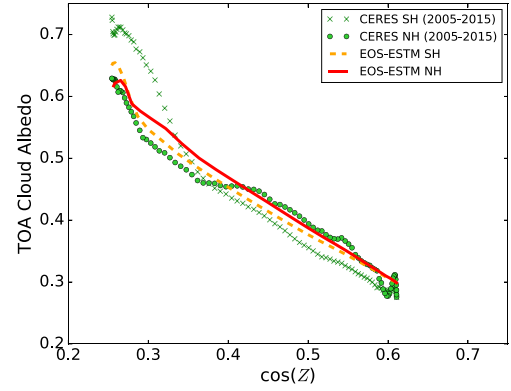
Figure 6. Cloud albedo versus $\mu = \cos Z$ for the present-day Earth (Northern and Southern hemispheres). Dark green circles and crosses: observational data obtained from equation (10) for the Northern and Southern hemisphere, respectively. Red-solid and orange-dashed lines: ESTM predictions obtained by converting to TOA values the cloud albedo calculated from equation (12) for the Northern and Southern hemisphere, respectively.

temperatures, ΔT_{max}, becomes smaller. A small time lag between the predicted and observed peak is also present and increases with decreasing C_{ml}. The value of thermal capacity that better reproduces the observed trend is found at $C_{ml} \simeq C_{ml50}/2$. We therefore adopt this value, which provides a small time lag and a difference of only 0.8 K between the observed and predicted value of ΔT_{max}.

3.1.6 Cloud albedo parameters

To tune the cloud albedo parameters $a_c(0.5)$ and m_c in equation (11), we used the TOA cloud albedo estimated from satellite data with equation (10). The corresponding model predictions were then calculated by applying the EOS radiative transfer calculations to the effective cloud albedo at the bottom of the atmosphere estimated with equation (12). In this process, we fine-tuned the cloud transmittance defined in equation(13). In Fig. 6, we compare the observational data set (green circles) with the final result of this modellization (orange curve). One can see that the new calibration of cloud albedo provides a good match to the measured trend of TOA cloud albedo versus μ, including the sharp rise observed at low μ, i.e. over the Earth polar caps. From this figure it is clear that the reflectivity of the underlying surface becomes fundamental at the poles. The previous version of the ESTM is unable to reproduce these features.

3.2 Diagnostic tests of the Earth model

To test the predictions of Earth model, we first investigated the temperature dependence of two key energy balance quantities, namely the OLR and TOA albedo. We then compare global and zonal planetary data with the model predictions.

3.2.1 OLR and TOA albedo

In Fig. 7, we plot the OLR (left-hand panel) and TOA albedo (right-hand panel) versus surface T obtained from the Earth's reference model (black lines) and Earth's satellite data (green circles). To obtain these plots, we plotted the mean annual OLR and TOA albedo of each latitude zone versus the corresponding zonal value of mean annual surface temperature. With this procedure, we obtain
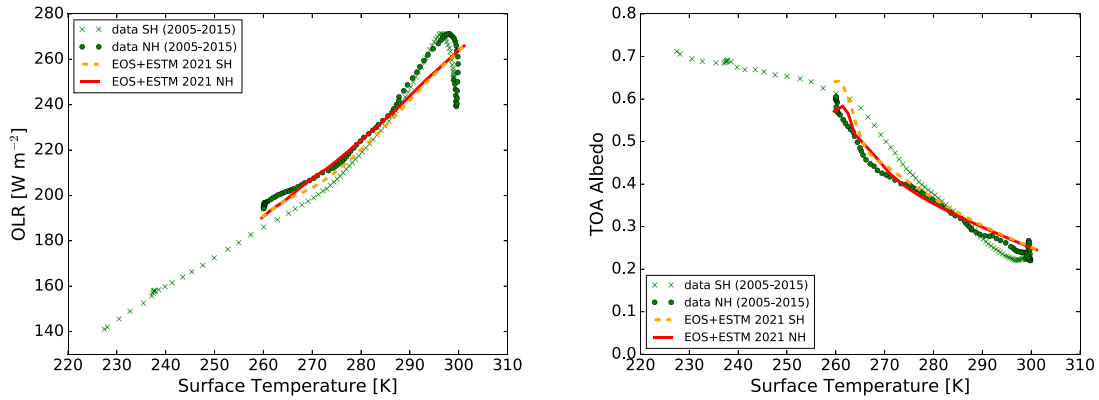
Figure 7. Mean annual values of OLR (left-hand panel) and TOA albedo (right-hand panel) plotted versus surface temperature for the present-day Earth. Data at temperatures below 260 K are related to the South Polar cap. Green dots and crosses: observational data obtained with the ERA5 reanalysis and CERES-EBAF satellite data averaged over the period 2005–2015, for the Northern and Southern hemisphere, respectively. Red-solid and orange-dashed lines: predictions of the Earth's reference model obtained with the radiative transfer calculations specified in Section 3.1.3, for the Northern and Southern hemisphere, respectively. The OLR peak at $\simeq 296$ K in the left-hand panel is due to emission at the edges of tropical regions, which are connected with the presence of large deserts and of low clouds with warm tops; the decrease around the equator is associated with the presence of deep convective clouds with cold tops.

two independent sets of data versus T, one for the Northern and the other for the Southern hemisphere. One can see that the EOS-ESTM calculations match well the Earth data, despite the simplified nature of the model. The agreement is better in the Northern hemisphere, which is less affected by the peculiar orography of Antarctica. A better match would require a 3D climate model with orography and a physical description of the atmospheric and oceanic fluidodynamics and clouds.

3.2.2 Global and zonal data

In Table 6, we display the globally averaged values of planetary quantities predicted by the Earth's reference model (second to last column). The comparison with the corresponding experimental data (previous column) shows an excellent agreement, with relative differences below 2 per cent for the albedo and much smaller for the temperature and OLR. The match of model and observed data is particularly good in the Northern hemisphere. The experimental data of the Southern hemisphere are significantly influenced by the high altitude of Anctartica, which is not accounted in our model without orography.

In Fig. 8, we compare the mean annual zonal values of surface temperature, TOA albedo, OLR, and ice cover obtained from the reference Earth model (solid lines) and Earth's satellite and reanalysis data (symbols). The agreement of the surface temperature curve (top left panel) is excellent, with an area-weighted rms deviation of 1.0 K for the Northern hemisphere. The main difference arise above the South Polar cap, where the observed temperature is ∼20 K lower than predicted due to the lack of orography of the model. This difference is consistent with the ∼2 km thickness of the ice sheet and a dry lapse rate of $\simeq 10$ K/km.

The albedo curve (top right panel) shows an excellent agreement in the Northern hemisphere at mid-high latitudes, where the gradual change of the albedo of transient ice provided by equations (5) and (6) yields a better match to the data than in the original ESTM. In the equatorial regions the agreement is reasonable, considering the existence of albedo factors that can only be treated in 3D models, such as the atmospheric circulation, which affects the clouds distribution. In the Antarctic region, the model underestimates the albedo due to the lack of orography.

The OLR profile (bottom left panel) shows a general agreement, with strong deviations in Antarctica and in the tropical regions. The OLR excess predicted by the model over Antarctic regions is due to the temperature excess that we have already discussed. The bumps of OLR emission measured at the edges of tropical regions are connected with the presence of large deserts and of low clouds with warm tops, while the reduced equatorial OLR is connected with the presence of deep convective clouds with cold tops (e.g. Hartmann 2016). Neither of these two features can be captured by our model which performs a sort of average that provides the correct global value of OLR (Table 6). The good match between model and observations in the North polar region is an improvement with respect to the original ESTM, and is due to the fact that the scaling factor (14) rises the planetary OLR emitted from frozen regions.

In the bottom right panel, we show a diagnostic test on ice coverage that was not performed by V15. The mean annual zonal coverage of ice predicted is in general agreement with the area-weighted lands and oceans data (red dots). This implies that the new algorithm that we have introduced, based on equation (4), is able to capture the main characteristics of ice coverage, using the dependence on a single parameter, namely the surface temperature. A treatment of the physics of ice formation and melting is, at this moment, beyond the scope of our model.

4 TESTING NON-TERRESTRIAL CONDITIONS

By changing the input parameters that describe the stellar, orbital, and planetary properties, the ESTM can be in principle applied to simulate a broad spectrum of exoplanetary climates. In this context, validation tests are required to assess the limits of validity of the model in non-terrestrial conditions. At present time, however, the climate systems of exoplanets are poorly constrained by observations and of no use for validating the model. Given this situation, the best way to test EOS-ESTM is to perform a comparison with the predictions obtained by other models that have been developed to investigate non-terrestrial planetary climates. Of particular interest is the comparison with 3D and 1D climate models, given the fact that ESTM is a 2D model, in the sense that we have clarified in Section 2. Below we provide the results of some preliminary comparison tests, starting from a simple simulation that we have performed using a
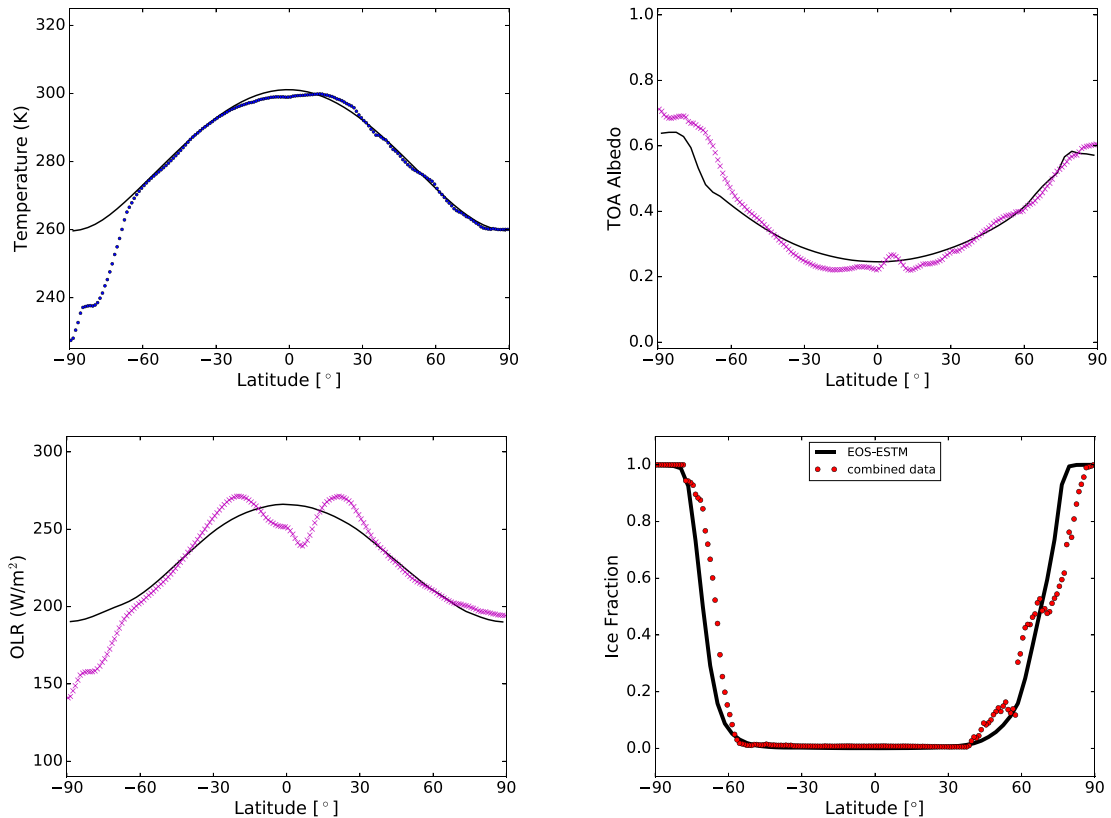
Figure 8. Mean annual latitude profile of surface temperature, albedo, outgoing longwave radiation (OLR), and fractional ice coverage predicted by the reference Earth model (solid lines). Top left panel: the temperature profile is compared with ERA5 temperatures averaged in the period 2005–2015 (blue dots). Top right panel: the albedo profile is compared with CERES-EBAF data averaged in the period 2005–2015 (pink crosses). Bottom left panel: the OLR profile is compared with CERES-EBAF data averaged in the period 2005–2015 (pink crosses). Bottom right panel: the model profile is compared with the mean ice coverage, obtained by weighting the land and ocean data (averaged in the period 2005–2015) in each zone according to the zonal coverage of lands and oceans.

3D model of intermediate complexity. We then describe several tests that we performed using predictions published in the literature. So far, the space of stellar/planetary parameters that affects exoplanetary climates has been covered only partially in previous work. Therefore, a comparison of different model predictions is only possible for a limited number of cases. Here, we focus our attention on the models and published results summarized in Table 10.

4.1 Earth-like aquaplanet

As a preliminary comparison test with a 3D climate model, we used the global climate model of intermediate complexity, PlaSim (Fraedrich et al. 2005; Angeloni, Palazzi & von Hardenberg 2020). Specifically, we tested the case of an aquaplanet with rotational spin aligned with the orbital spin ($\epsilon = 0$), the remaining parameters being equal to those of the Earth. For the sake of comparison with EOS-ESTM, the PlaSim simulation was run without oceanic transport. The resulting mean annual latitude profiles of surface temperature and top-of-atmosphere albedo are shown in Fig. 9. Despite the 3D nature of PlaSim and the different prescriptions of surface features, clouds, and ice between the two models, one can see that the results are in general agreement. This is true, in particular, for the temperature profile (left-hand panel). The differences found in the albedo profiles (right panel) are due to the cloud distribution, which follows the atmospheric circulation pattern that can be modelled in PlaSim, but not in EOS-ESTM.

Setting PlaSim parameters to non-terrestrial conditions is not trivial. This is true, in general, for all 3D models, particularly for the most complex ones. For this reason, extending the comparison tests with PlaSim to cover a broader space of parameters will be the subject of a separate work.

4.2 Variations of stellar insolation

To test the model response to variations of insolation, S, we run a set of simulations aimed at reproducing similar climate experiments performed with 1D (Godolt et al. 2016) and 3D models (Leconte et al. 2013; Shields et al. 2014; Wolf & Toon 2014, 2015). In all cases, an Earth-like atmosphere was considered, with properties described in Table 10.

The comparison with the 1D model is shown in Fig. 10, where we plot the mean surface temperature as a function of S for two cases considered by Godolt et al. (2016). The first case (left-hand panel) is a cloud-free Earth-like planet with a fixed albedo $A_{surf} = 0.22$, a value that, according to Godolt et al. (2016), reproduces the mean surface temperature of Earth in a cloud-free model. The second case (right-hand panel) is an Earth-like aquaplanet with $A_{surf} = 0.07$, as adopted by Godolt et al. (2016), which is representative of the ocean albedo. In both cases ice was not considered. One can see that, despite the existence of some differences in the parametrizations (Table 10), the EOS-ESTM results (red solid lines) are in good agreement with those provided by Godolt et al. (2016) (black solid lines). Departures

Table 10. Summary of the test cases represented in Figs 10, 11, and 12. The second and third columns give the radiative transfer (RT) model and the atmospheric properties adopted. The last column reports the references. Kunze et al. (2014) adopted the RAD4ALL model (Nissen et al. 2007) for the shortwave transport and the RRTM model (Mlawer et al. 1997) for the longwave transport.

Model Name	RT model	Atmosphere	Reference
ESTM	EOS	1.013 bar N_2, CO_2 (360 ppm), CH_4 (1.8 ppm) and H_2O	This work
1DGodolt2016	K84[20]	1 bar N_2, O_2, CO_2 (355 ppm), CH_4 (1.64 ppm), O_3 and H_2O	Godolt et al. (2016)
3DLeconte2013	LMDG	1 bar N_2, CO_2 (376 ppm), and H_2O	Leconte et al. (2013)
3DWolf&Toon2015	CAM 4	0.983 bar N_2, CO_2 (367 ppm), and H_2O	Wolf & Toon (2015)
3DWolf&Toon2014	CAM 3	0.983 bar N_2, CO_2 (367 ppm), and H_2O	Wolf & Toon (2014)
EBMShields+2013	SMART	present-day Earth CO_2, O_2 and H_2O	Shields et al. (2013)

[20]Kasting, Pollack & Crisp (1984)
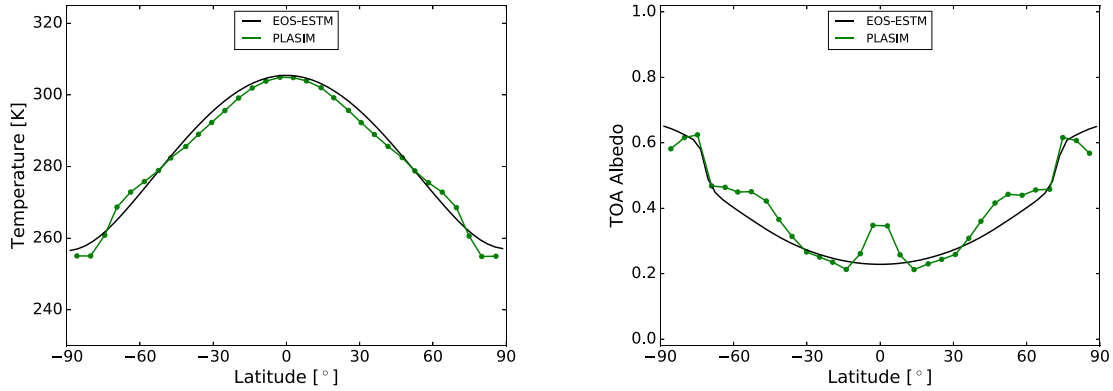
Figure 9. Comparison of model predictions obtained for an Earth-like aquaplanet using the EOS-ESTM (black curves) and the 3D climate of intermediate complexity PlaSim (green curves). Left-hand panel: mean annual surface temperature versus latitude. Right-hand panel: mean annual top-of-atmosphere albedo versus latitude. See Section 4.1.
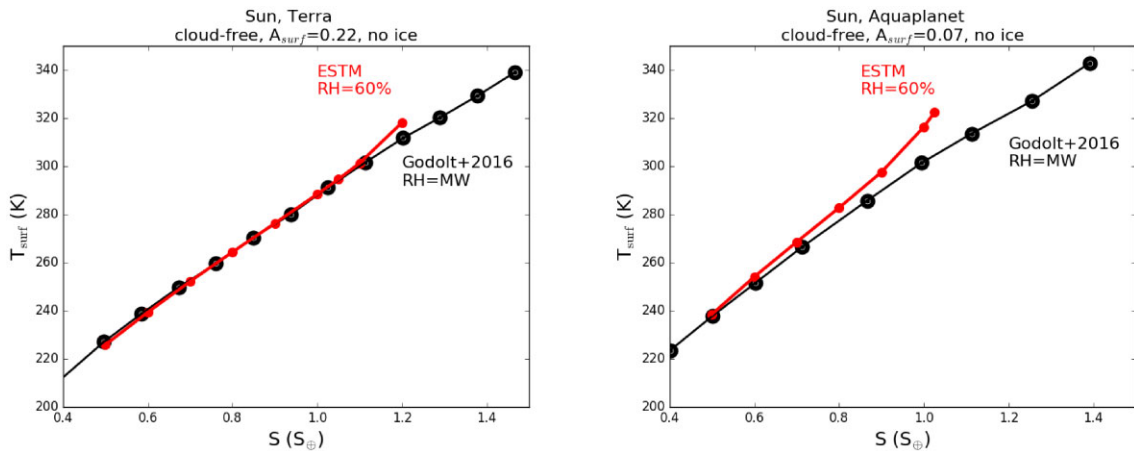
Figure 10. Surface temperatures an Earth-like planet (left-hand panel) and of an aquaplanet (right-hand panel) orbiting a Sun-like star at various stellar insolations, *S*. In both cases, a cloud-free configuration is considered with no ice formation and a fixed value of surface albedo: 0.22 (left-hand panel) and 0.07 (right-hand panel). Black solid line: results obtained by Godolt et al. (2016) with a 1D model with relative humidity specified by Manabe & Wetherald (1967). Red solid line: results obtained in this work, where we adopt RH = 60 per cent.

between the models arise for high values of surface temperatures. This effect is emphasized in the aquaplanet scenario, where the deviations start to be present above ∼280 K (right-hand panel). Since the differences become important at high temperature, when the atmospheres contain more water vapor, this effect may be induced by a different treatment of the relative humidity (RH). Indeed, in our model we adopt a constant value, RH = 60 per cent, representative of the mean global value of the Earth, whereas Godolt et al. (2016) used a parametrization proposed by Manabe & Wetherald (1967), representative of the RH vertical profile of the Earth.

In Fig. 11, we compare the mean annual global surface temperature (left-hand panel) and TOA albedo (right-hand panel) obtained with the 3D climate models. When the increase of insolation is modest, the results obtained with our model (red line) are in general agreement with those provided by the 3D models. However, discrepancies with Leconte et al. (2013) (green solid lines) and Wolf & Toon (2015) (black solid lines) appear at higher insolation, when the surface temperature rises above ∼290 K. Important differences are likely to arise from the different RT model adopted (Table 10). As shown in Simonetti et al. (2022, fig. 10a therein) and in Yang et al. (2016, fig. 3a therein), differences in the impact of the water vapor absorption predicted by different RT models start to become important for temperatures higher than 290 K. In particular, due to the onset of the runaway greenhouse instability, the slope of the OLR versus T_{surf} in the CAM4 and LMDG models flattens more than in EOS. Therefore, under equal insolation conditions, EOS-ESTM features lower surface temperatures. On the other hand, the CAM3 model (solid cyan line) exhibits a lower surface temperature in response to higher insolations. We believe that this behaviour can be associated with the temperature dependence of the OLR and TOA albedo. In fact, for temperatures above ∼300 K, the CAM3 model features the largest value of OLR (Simonetti et al. 2022, fig. 10a therein) and, at the same time, a slightly higher TOA albedo compared to other models (Simonetti et al. 2022, fig. 10b therein).

Besides the different RT recipes, deviations in the predictions are expected because our model does not incorporate a 3D physical treatment of the cloud and water vapor feedbacks, even though it does reproduce the essential features of the ice-albedo feedback and, to some extent, the rise of water vapour with temperature. We suggest that the sharp transitions of surface temperature (left-hand panel) and TOA albedo (right-hand panel) found by Leconte et al. (2013) and Wolf & Toon (2015) can be associated with variations in the cloud fraction in response to the increase of insolation. This interpretation is consistent with the fact that such transitions are not found for the surface albedo (dashed lines, right-hand panel), for which the cloud/atmospheric effects are not relevant.

4.3 Variation of stellar spectra

The ice-albedo feedback is a well known mechanism that affects the planetary climate with a de-stabilizing effect that, in the most extreme cases, may lead to an ice-covered planetary state, called 'snowball' (Kirschvink 1992). Owing to the wavelength dependence of the albedo, the impact of this effect will depend on the spectral energy distribution (SED) of the central star. G-type stars, like our Sun, emit a far greater fraction of their radiation in the visible light spectrum, whereas smaller and cooler M-dwarfs exhibit their peak output in the ∼0.8 to 1.2 μm range (Shields et al. 2013, fig. 1a therein). The fact that these stars emit a significant fraction of their radiation above 1 μm, combined to the reduction of the albedos of snow and ice at the same wavelengths (Shields et al. 2013, fig. 1b therein), implies that the albedos of frozen surfaces are lower on

planets orbiting M-type stars than on Earth. Calculations of broad-band albedo,[21] performed taking into account the stellar SEDs and the wavelength-dependence albedo of snow and ice, indicate that the ice-albedo feedback is weaker around M-type stars (Joshi & Haberle 2012). The atmospheric contribution to the albedo in these stars was studied by Von Paris et al. (2013): the presence of trace amounts of H_2O and CH_4 in the atmosphere, as well as high CO_2 pressures, damps the ice-albedo feedback in planets around M-type stars.

To test the EOS-ESTM predictions at different stellar SEDs, we performed a comparison with the work by Shields et al. (2013). These authors used a 1D radiative transfer model (SMART) to calculate the broad-band planetary albedo, given the spectrum of the central star and that of the surface albedo. Then, they included the resulting broad-band albedo into a 1D EBM to calculate the mean global surface temperature as a function of insolation for an aquaplanet orbiting a G-type star (the Sun) and an M-type star (AD Leo). Following their prescriptions, we considered an aquaplanet with an axis obliquity of 23°, zero orbital eccentricity and a present-day Earth atmospheric composition. For consistency with their work, we considered a spectral distribution representative of AD Leo, which is a M3.5-type star, with a $M_{\star} = 0.42 \, M_{\odot}$ (Reiners, Basri & Browning 2009). Since at decreasing insolation the aquaplanet undergoes a transition towards a 'snowball' state, we dedicate special attention to select the value of the albedo of ice over ocean, a_{io}. Among the different values of 'blue ice'[22] calculated by Shields et al. (2013, table 2), we adopt the value for the case with no gases and clouds and no Rayleigh scattering. This is the case more appropriate for the surface albedo in our model, since the EOS-ESTM calculates the contribution of the atmosphere and clouds in its own way. The results are shown in Fig. 12, where the planet orbiting the M-type dwarf appears less susceptible to 'snowball' states, since the ice is particularly absorptive in the NIR, as well as the atmosphere. In spite of small differences associated with the transition to a complete 'snowball' state, expressed as a sudden decrease of global surface temperature, the results obtained with EOS-ESTM (red lines) and by Shields et al. (2013) (black line) show an overall agreement. The main difference between the trends found in the two models may arises from the different parametrization of ice: the smooth transition in our model is probably due the gradual temperature dependence of the ice coverage described in Section 2.3.

4.4 Variations of planet radius and rotation rate

A critical difference between ESTM and GCMs is the treatment of the meridional transport. As explained in V15 (see Section 2.1), we model the D term in equation (1) as a scaling relation between planetary quantities that are involved in the physics of the meridional transport. To test the reliability of this parametrization, we run a set of simulations varying one parameter at a time and compared our results with similar tests performed with GCMs by other authors. Specifically, we varied the planetary radius and rotation rate and performed a comparison with results published by Kaspi & Showman (2015) and Komacek & Abbot (2019).

The mean annual equator-to-pole temperature difference, ΔT_{EP}, is a good indicator of the efficiency of the meridional transport and is expected to be higher in planets with fast rotational velocities or

---

[21]The ratio of the surface upward radiation flux to the downward radiation flux within a certain wavelength range (Kokhanovsky 2021).

[22]According to Shields et al. (2013), blue marine ice results from freezing of liquid marine water and not from glacier ice.
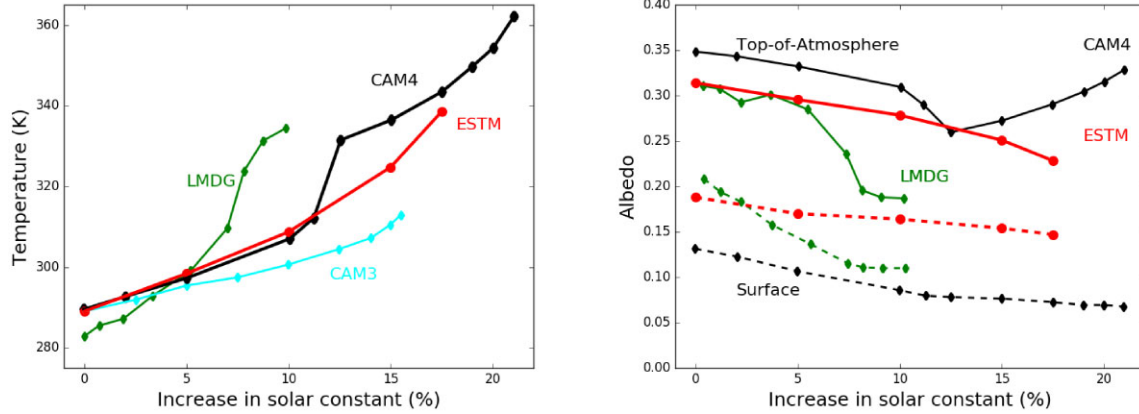
Figure 11. Comparison of global and annual mean surface temperature (left-hand panel) and TOA albedo (right-hand panel) obtained from different climate Earth's models by increasing the solar constant. Red, solid line: EOS-ESTM (this work). Black, solid line: 3D model CAM4 (Wolf & Toon 2015). Green solid line: 3D model by Leconte et al. (2013). Dashed lines in the right-hand panel represent the surface albedo of these three models, indicated with the same colour coding.
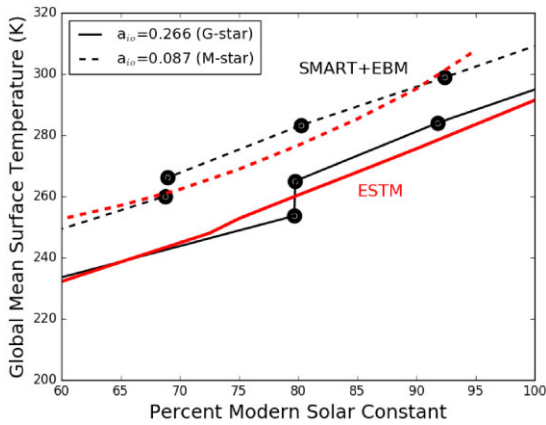
Figure 12. Mean global surface temperature versus stellar flux for an aquaplanet orbiting an M-type (dashed lines) and a G-type (solid lines) star. Due to the different stellar SED, the albedo of ice over the ocean, a_{io}, is varied as indicated in the legenda. Black lines: predictions obtained by Shields et al. (2013) with SMART in combination with an EBM adapted from North & Coakley (1979). Red lines: results obtained in this work adopting a warm start for consistency with Shields et al. (2013).

large radii. The Coriolis forces resulting from planetary rotation tend to inhibit the transport from the tropics to the poles, leading to a higher gradient ΔT_{EP}. Quantifying these effects with 3D models is important because changes of rotational angular velocity may affect the location of the inner edge of the habitable zone (Yang et al. 2014; Yang, Komacek & Abbot 2019). Also variations of planetary radius affect the meridional gradient: as the radius increases, so does the physical distance between equator and poles, leading to a less efficient meridional heat distribution, i.e. a larger ΔT_{EP}. In Fig. 13, we show how ΔT_{EP} is predicted to change as a function of planetary radius (left-hand panels) and rotation period (right-hand panels) for different models that we describe below. Following Komacek & Abbot (2019), we normalize ΔT_{EP} to the values predicted by each model for Earth's values of rotation rate and radius. The results obtained by Kaspi & Showman (2015) and Komacek & Abbot (2019) are rather different, despite both being based on 3D models. We refer to the latter paper for a discussion on these differences, which may be due to different physico-chemical assumptions and to the fact that

the model of Komacek & Abbot (2019) had not been tuned to match the Earth. Here, we compare our results with those obtained in these two papers.

4.4.1 Comparison with Kaspi & Showman (2015)

To investigate the atmospheric dynamics over a wide range of planetary parameter space, Kaspi & Showman (2015) adopted a 3D GCM with a scheme similar to that of Frierson, Held & Zurita-Gotor (2006) both for the radiative transfer and the surface boundary-layer: a standard two-stream grey radiation and an uniform 1-m water-covered slab, with an albedo of $A = 0.35$, respectively. They modelled an idealized aquaplanet at perpetual equinox with an Earth-like reference atmosphere. The effects of clouds, sea-ices, and continents were not accounted for. For the sake of comparison, we adopted the same set of conditions in EOS-ESTM. In the top panels of Fig. 13 one can see that, in spite of differences at the low- and high-radius and rotation rate regimes, the EOS-ESTM predictions (red symbols and lines) reproduce the trends obtained by Kaspi & Showman (2015) with the 3D aquaplanet (blue symbols and lines). The two sets of results are consistent as long as the planets have radii and rotation rates sufficiently close to those of the Earth. For habitability studies, we are interested in the range of radii expected for rocky planets, shown as shaded red areas in the left-hand panels of Fig. 13. In this range, the predictions of the two models are comparable.

4.4.2 Comparison with Komacek & Abbot (2019)

More recently, Komacek & Abbot (2019) investigated how the atmospheric circulation and climate of planets orbiting Sun-like stars vary when planetary parameters are changed. They used the state-of-the-art GCM ExoCAM (a modified version of the Community Atmosphere Model version 4), to simulate an idealized aquaplanet with a 50-m water slab without oceanic transport and an atmosphere of N_2 and H_2O. At variance with Kaspi & Showman (2015), they included the effects of clouds, non-grey radiative transfer, and sea ice. To test the EOS-ESTM predictions making use of their results, we adopted, for consistency, a uniform 50-m thick water-covered slab, the same atmosphere of N_2 and H_2O, and the same ice albedo; we set to zero both the axis obliquity and orbital eccentricity. In the bottom panels of Fig. 13, we compare the normalized ΔT_{EP} obtained with
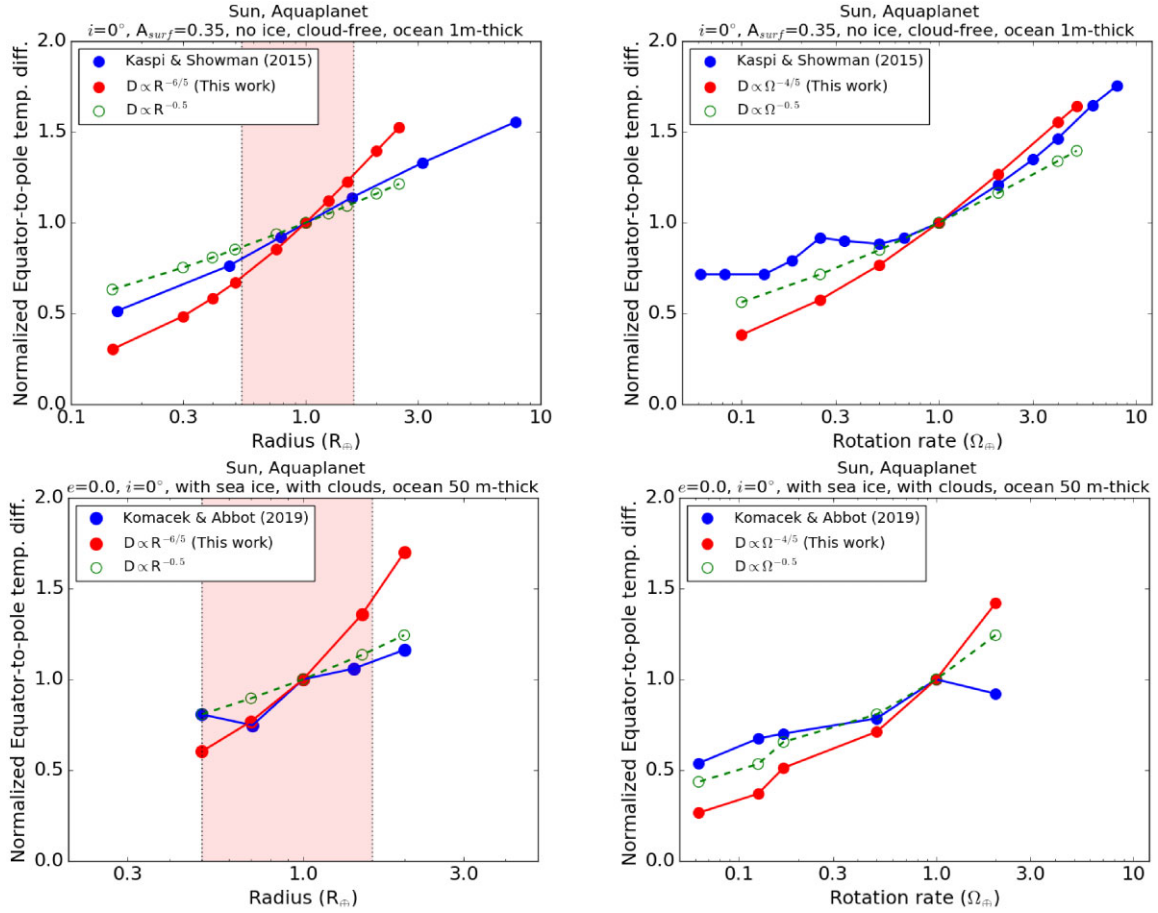
Figure 13. Normalized equator-to-pole temperature difference as a function of planet radius (left-hand panels) and planet rotation rate (right-hand panels) for an Earth-like aquaplanet. *Top panels*: comparison between the results obtained in this work (red lines) and those obtained by Kaspi & Showman (2015) (blue lines) for a cloud-free aquaplanet slab ocean with a depth of 1 m, an axis obliquity $i = 0°$, a fixed albedo (A = 0.35), and no sea ice. *Bottom panels*: comparison between the results obtained in this work (red lines) and by Komacek & Abbot (2019) (blue lines) for an aquaplanet slab ocean with a depth of 50 m where the effects of clouds, non-grey radiative transfer, and sea ice are included; axis obliquity $i = 0$ and the eccentricity $e = 0$. *Shaded red area*: range of radius ($0.5 <$ R/R$_\oplus < 1.6$) at which an exoplanet is more likely to be composed of rock and metal (Meadows & Barnes 2018).

our model (red symbols and lines) with those obtained with the GCM (blue symbols and lines).

In the bottom left panel one can see that the trend of increasing $\Delta T_{\rm EP}$ that we find (red line) is consistent, but steeper than that found with the GCM (blue line), the departures becoming significant above the radius limit of rocky planets. The smoother trend found with the GCM suggests that the large scale, 3D circulation, not present in our model, may enhance the heat distribution. Our trend is somewhat steeper than the one that we found in the previous test (top left panel), indicating how the inclusion of clouds and ice impacts our results.

The bottom right panel of Fig. 13 shows a consistent trend for angular velocity lower than $\Omega_\oplus$, with a discrepancy at high angular velocity ($\Omega = 2 \ \Omega_\oplus$). This discrepancy is surprising, because our algorithm for meridional transport is expected to be more realistic for fast-rotating planets (see V15), and this indication is supported by the comparison with Kaspi & Showman (2015) shown in the top right panel. Clearly, the two 3D models that we are using for comparison show remarkable differences between them and should be taken with some caution. At low rotation speed, where we know that our assumptions are more critical (see V15), our model seems to underestimate $\Delta T_{\rm EP}$, as in the comparison with Kaspi & Showman (2015) shown in the top right panel. These results suggest that the

3D circulation may be able to redistribute the heat efficiently, with a weak dependence on the planet rotation rate.

4.4.3 Future improvements of the model

In our parametrization of the meridional transport, the term D scales as $\Omega^{-4/5}$ and $R^{-6/5}$ (see V15, Section 2.1). Taking advantage of the flexibility of our model, we varied the exponents of these power laws, searching for a better agreement with the trends obtained by the 3D models shown in Fig. 13. The dashed green lines plotted in all panels of that figure show that a better match with the 3D results is achieved when adopting a more moderate dependence for both the angular velocity, $\propto\Omega^{-0.5}$ and radius, $\propto R^{-0.5}$. This exercise shows that, in principle, one could recalibrate the exponents of the scaling relations that we adopt for D, making use of specifically designed tests performed with GCMs. To this end it would be important to use realistic 3D models for cross-validation. Realistic models should include the main components of the climate system and should be calibrated to match the Earth data. Setting state-of-the-art GCM models to simulate non-terrestrial conditions is not a straightforward task. However, this is the way to proceed for expanding the range of application of flexible models such as

EOS-ESTM and exploring the parameter space that allows habitable climates to exist.

4.5 The outer edge of the habitable zone

In classic studies of the HZ, the locations of the inner and outer edge are calculated making use of single-column, cloud-free atmospheric climate models (Kasting et al. 1993; Kopparapu et al. 2013a). In recent years, several studies have proven the critical role of planetary properties on the position and extension of the circumstellar HZ (Yang et al. 2014; Rushby, Shields & Joshi 2019; Yang et al. 2019; Zhao et al. 2021). Here, we take advantage of the flexibility of EOS-ESTM to investigate how the location of the outer edge is affected by variations of planetary parameters. Establishing the exact location of the outer edge would require a study of clouds effects (e.g. Forget & Pierrehumbert 1997; Selsis et al. 2007; Kitzmann 2017) and the possible presence of other greenhouse gases, such as CH_4 (see Ramirez & Kaltenegger 2018). However, for the climate experiments that we present here, we simply adopt the 'maximum greenhouse' limit, defined as the maximum distance at which a cloud-free planet with an atmosphere dominated by CO_2 can maintain a surface temperature of 273 K (Kasting et al. 1993). Beyond this limit, the greenhouse effect due to a further rise of CO_2 is offset by the rise of atmospheric albedo due to the Rayleigh scattering of CO_2 molecules. To explore the impact of planetary parameters on the location of the outer edge, we considered a cloud-free, CO_2-dominated atmosphere with a dry surface pressure of 7.3 bar,[23] which is the value identified by Kopparapu et al. (2013a) as the maximum greenhouse limit. To build the pressure–temperature profile of the atmosphere, we followed the recipes in the appendix of Kasting (1991), with an H_2O-saturated lower troposphere, a CO_2-saturated upper troposphere and a 154 K isothermal stratosphere. We varied the insolation of a planet with Earth-like parameters and solar-type central star, searching for the limit at which the planet undergoes a transition to a snowball state.

For simplicity, we considered only the solutions obtained with warm initial conditions, i.e. starting with $T_0 = 300$ K, which provide a conservative outer limit to the habitable zone.

The results of these experiments are shown in Fig. 14, where we plot the mean-annual global ice coverage as a function of insolation obtained for different values of planetary rotation, radius, axis tilt, and ocean/land distribution. In all cases we find that the transition to a snowball state is rather sharp, taking place around $\simeq 1.6$ au. This result is in general agreement with the maximum greenhouse limit for a solar-type star found at 1.67 au by Kasting et al. (1993) and Kopparapu, Ramirez & Kasting (2013b) from single-column calculations. The different treatment of the radiative transfer and of the climate recipes in our model can explain why we find the snowball transition at a location somewhat closer to the star than the classic outer edge. In particular, we used more recent spectral data (HITRAN2016) and a different H_2O continuum model with respect to Kasting et al. (1993) and Kopparapu et al. (2013a). Our RT calculations employed a more coarse vertical pressure grid with respect of Kopparapu et al. (2013a), which is known to slightly increase the OLR (thus increasing the lower insolation limit). Finally, we adopted less opaque CIA prescriptions for the CO_2 with respect to Kasting et al. (1993), which are considered more in line with

experimental results (see Wordsworth, Forget & Eymet 2010, for a discussion on the subject).

The extra dimension (latitude) and the ice-albedo feedback that are present in our model provide a detailed description of the climate changes that take place in the proximity of the outer edge. A detailed analysis of Fig. 14 highlights the role played by different planetary properties in determining the onset of the snowball transition. In the top left panel, one can see that the transition occurs at increasing distance from the star when the rotation period increases. This effect is expected because the heat transport from the equator to the poles becomes more efficient with increasing P_{rot}, leading to a slower growth of the ice polar caps. In the top right panel, one can see that the increase of planetary radius shifts the snowball boundary inwards. This is due to the fact that the heat transport to the poles is less effective in planets with larger R_p, leading to a faster growth of the polar caps. The bottom left panel shows that an increase of the planetary axis tilt, ϵ, shifts the snowball limit outwards. The effect is negligible up to $\epsilon \simeq 20°$, becoming evident above $\simeq 30°$. In this moderate range of obliquities, the effect can be interpreted as follows. The configuration at $\epsilon = 0°$ favours the formation of permanent ice caps in the polar regions, where the zenith distance Z is always large. As the obliquity starts to increase, the polar regions undergo a period of higher insolation (lower Z) in some seasons, which tends to reduce the ice caps. At very high obliquities the behaviour is more complex (see section 4.4.2 in V13) and can be properly investigated only using 3D models.

In the bottom panel of Fig. 14, we show the impact of variations of ocean/land distribution. As one can see, the outer limit shifts outwards when the fraction of oceans, f_o, increases. The land planet, with $f_o = 0.05$, provides an extreme example of early snowball transition. These results can be understood in terms of the lower albedo and higher thermal capacity of the oceans compared to the continents. The snowball transition that we find is slightly sharper in ocean planets than in desert planets owing to the slightly different temperature dependence of ice over oceans and lands (Section 2.3). Our results are in line with recent findings that planets covered largely by oceans have warmer average surface temperatures than land-covered planets Rushby et al. (2019).

5 CONCLUSIONS

We have presented EOS-ESTM, a flexible climate model aimed at simulating the surface and atmospheric conditions that characterize habitable planets. The model allows one to perform a fast exploration of the parameter space representative of planetary quantities, including those currently not measurable in rocky exoplanets. EOS-ESTM has been built up starting from ESTM, a seasonal-latitudinal EBM featuring an advanced treatment of surface and cloud components and a 2D (vertical and latitudinal) treatment of the energy transport. The main upgrades of EOS-ESTM can be summarized as follows:

(i) The atmospheric radiative transfer is calculated using EOS (Simonetti et al. 2022), a procedure tailored for atmospheres of terrestrial-type planets, based on the opacity calculator HELIOS-K (Grimm & Heng 2015; Grimm et al. 2021) and the radiative transfer code HELIOS (Malik et al. 2017, 2019). Thanks to EOS, the ESTM radiative transfer can be now calculated for a variety of atmospheres with different bulk and greenhouse compositions, illuminated by stars with different SEDs.

(ii) The parametrizations that describe the clouds properties have been largely upgraded. New equations have been introduced for the albedo of the clouds and its dependence on the albedo of the

---

[23]Kopparapu and collaborators also had an additional bar of N_2 in all their models, thus they evaluated the CO_2 *partial* pressure. Taken alone, it would produce a surface pressure of 7.3 bar.
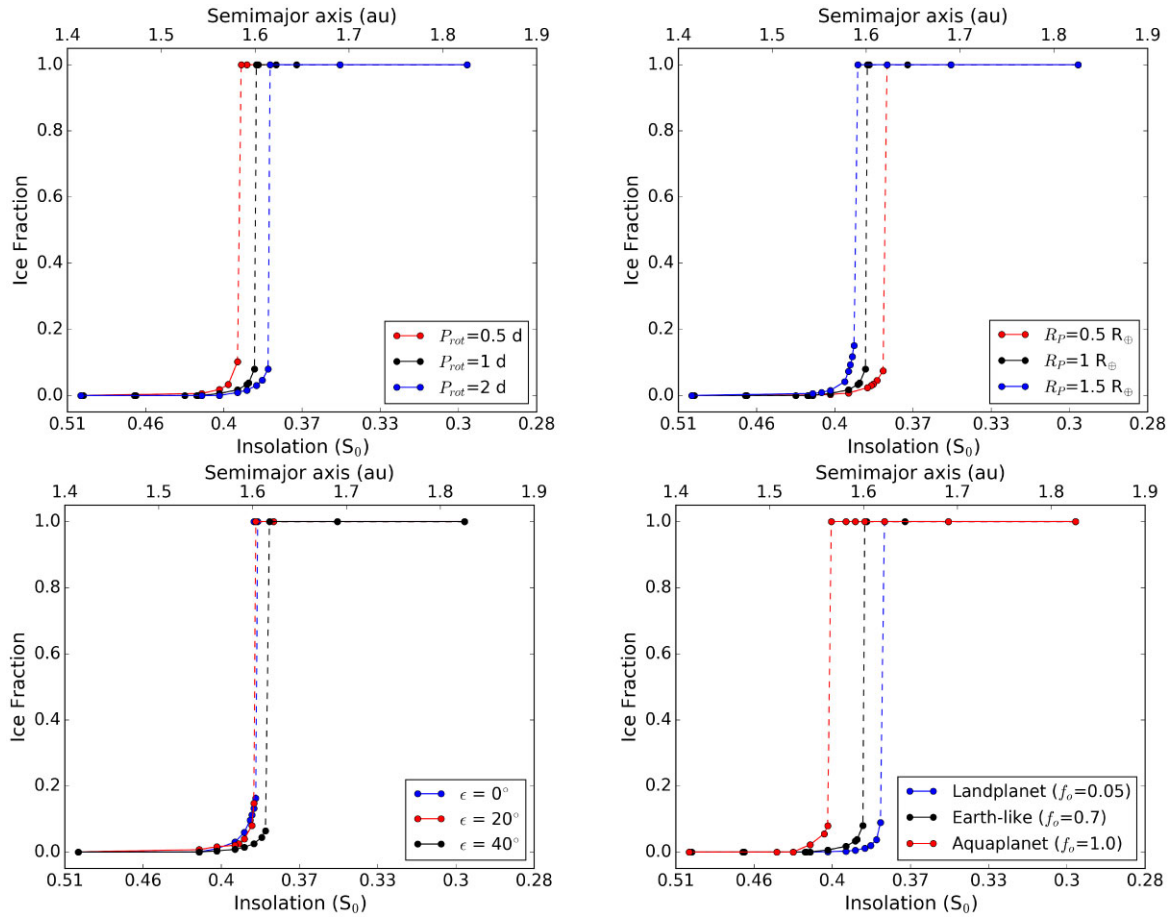
Figure 14. Dependence on planetary parameters of the fractional ice coverage calculated at the outer edge of the HZ. The results were obtained for a cloud-free Earth-like planet with a CO_2-dominated, maximum greenhouse atmosphere, the remaining parameters being fixed to Earth values; only the solutions obtained with warm initial conditions ($T_0 = 300$ K) are shown (see Section 4.5). Top left panel: rotation period, P_{rot}; top right panel: planet radius, R_p; bottom left panel: axis obliquity, ϵ; bottom right panel: geography.

underlying surface. The clouds coverage over ice is now a function of the global planetary ice coverage. A specific treatment for the transmittance and OLR forcing of clouds at very low temperature has been introduced.

(iii) A generalized logistic function has been introduced to estimate the ice coverage as a function of mean zonal surface temperature. Based on a detailed study of the ice distribution on Earth, the adopted algorithm discriminates between ice over lands and oceans. The albedo and thermal capacity of transitional ice is now estimated using the fractional ice coverage.

With the aim of providing a reference model for studies of habitable planets, we calibrated EOS-ESTM using a large set of Earth satellite and reanalysis data. The reference Earth model satisfies a variety of diagnostic tests, including mean global measurements (Table 6) and mean latitudinal profiles of surface temperature, TOA albedo, OLR, and ice coverage (Fig. 8). The positive results of the diagnostic tests were obtained by tuning the parameters within narrow ranges perfectly consistent with measurements of each climate component. All the Earth's data used in our analysis were selected for the same period (2005–2015) and the atmospheric trace content of greenhouse gases was tuned accordingly (Section 3.1.3). Due to the lack of 3D treatment of clouds and atmospheric circulation, the model is not able to reproduce the detailed shape of the OLR

latitudinal profile, even though it does reproduce correctly the mean global value.

To test the consistency of EOS-ESTM with previous studies of non-terrestrial climate conditions, we performed a series of comparisons with a hierarchy of climate models (Section 4). The results of these tests can be summarized as follows:

(i) The latitudinal profiles of temperature and albedo of an Earth-like aquaplanet are in agreement with predictions obtained using the 3D, intermediate complexity model PlaSim. Differences that we find are due to the lack of the 3D atmospheric circulation and the 3D representation of clouds in our model.

(ii) Comparisons performed at varying levels of insolation yield results which are in general agreement with other models. However, critical differences appear at high insolation and temperature, when the resulting abundance of water vapour makes extremely model-dependent the radiative transfer calculations. Changing stellar spectrum at moderate and low levels of insolation yields consistent results.

(iii) Comparisons performed at varying planetary radius and rotation rate yield consistent results, but suggest that the dependence of the meridional transport on these planetary quantities may be more moderate than estimated in V15. This test indicates that some parameters of our model can be recalibrated using a proper set of climate experiments carried out with state-of-the-art GCMs.

(iv) The application of EOS-ESTM to the case of a CO_2-dominated atmosphere in maximum greenhouse conditions (Kasting et al. 1993) yields a detailed description of the transition to a snowball state that takes place when the insolation decreases in the proximity of the outer edge of the HZ. Thanks to the flexibility of our model, we can explore how this transition develops in different planetary conditions (e.g. rotation rate, radius, axis tilt, ocean coverage), taking also into account the presence of climate bistability.

The possibility to easily adapt the input parameters to simulate a broad spectrum of planetary and atmospheric quantities allows one to apply EOS-ESTM to simulate a large variety of terrestrial-type exoplanets. As in the case of the original ESTM, this flexibility can be used to explore in detail the habitability conditions of individual exoplanets (Silva et al. 2017b) or to perform statistical studies of exoplanetary habitability (Murante et al. 2020). With EOS-ESTM it will be possible to extend these types of studies with a more accurate treatment of the climate effects of land, oceans, ice and clouds, and expanding the palette of atmospheres to non-terrestrial compositions and the host stars to non-solar types.

The flexibility of EOS-ESTM paves the road for building up multiparameter habitable zones, each parameter being representative a planetary property that affects the climate. To achieve this ambitious goal it is important to assess the consistency with respect to a hierarchy of climate models, devising a dedicated series of experiments with the same set of initial conditions. Given the vastness of possibilities to be tested, a collaborative effort is required in order to establish proper protocols for a meaningful comparison of models developed by independent research groups, such as the TRAPPIST-1 Habitable Atmosphere Intercomparison (THAI, Fauchez et al. 2020, 2021a), and the future larger project Climates Using Interactive Suites of Intercomparisons Nested for Exoplanet Studies (CUISINES) NExSS[24] Working Group (Fauchez et al. 2021b).

ACKNOWLEDGEMENTS

DATA AVAILABILITY

The data used for this article will be shared on reasonable request to the corresponding author.

REFERENCES

Abbot D. S., 2014, J. Clim., 27, 4391
Angeloni M., Palazzi E., von Hardenberg J., 2020, Geosci. Model Dev. Discuss., 2020, 1
Barnes R., 2017, Celest. Mech. Dyn. Astron., 129, 509
Borucki W. J. et al., 2010, Science, 327, 977
Briegleb B. P., 1992, J. Geophys. Res., 97, 7603
Briegleb B. P., Minnis P., Ramanathan V., Harrison E., 1986, J. Appl. Meteorol., 25, 214
Broeg C., Benz W., Fortier A., 2018, 42nd COSPAR Scientific Assembly. p. E4.1–5-18

Cess R. D., 1976, J. Atmos. Sci., 33, 1831
Clough S. A., Shephard M. W., Mlawer E. J., Delamere J. S., Iacono M. J., Cady-Pereira K., Boukabara S., Brown P. D., 2005, J. Quant. Spectrosc. Radiat. Transfer, 91, 233
Coakley J., 2003, Encyclopedia of Atmospheric Sciences, p. 1914
Ellis J. S., Haar T. H. V., 1976, Zonal Average Earth Radiation Budget Measurements from Satellites for Climate Studies
Enomoto T., 2007, JAMSTEC Rep. Res. Dev., 6, 21
Fauchez T. J. et al., 2020, Geosci. Model Dev., 13, 707
Fauchez T. J. et al., 2021a, Planet. Sci. J., 2, 106
Fauchez T. et al., 2021b, BAAS, 1018
Forget F., Pierrehumbert R. T., 1997, Science, 278, 1273
Fraedrich K., Jansen H., Kirk E., Luksch U., Lunkeit F., 2005, Meteorol. Z., 14, 299
Frierson D. M. W., Held I. M., Zurita-Gotor P., 2006, J. Atmos. Sci., 63, 2548
Fujii Y. et al., 2018, Astrobiology, 18, 739
Fulton B. J. et al., 2017, AJ, 154, 109
Gardner J. P. et al., 2006, Space Sci. Rev., 123, 485
Gaudi B. S. et al., 2020, preprint (arXiv:2001.06683)
Godolt M., Grenfell J. L., Kitzmann D., Kunze M., Langematz U., Patzer A. B. C., Rauer H., Stracke B., 2016, A&A, 592, A36
Gordon I. E. et al., 2017, J. Quant. Spectrosc. Radiat. Transfer, 203, 3
Grimm S. L., Heng K., 2015, Astrophysics Source Code Library, record ascl:1503.004
Grimm S. L. et al., 2021, ApJS, 253, 30
Haqq-Misra J., Hayworth B. P. C., 2022, Planet. Sci. J., 3, 32
Hartmann D. L., 2016, Global Physical Climatology, 2nd edn., Elsevier, Boston
Hartmann D. L., Ockert-Bell M. E., Michelsen M. L., 1992, J. Clim., 5, 1281
Hersbach H. et al., 2020, Q. J. R. Meteorol. Soc., 146, 1999
Howard A. W. et al., 2012, ApJS, 201, 15
Huang C. J., Qiao F., Chen S., Xue Y., Guo J., 2019, J. Geophys. Res.: Oceans, 124, 4480
Jenkins J. M. et al., 2015, AJ, 150, 56
Joshi M. M., Haberle R. M., 2012, Astrobiology, 12, 3
Kalirai J., 2018, Contemp. Phys., 59, 251
Kaltenegger L., 2017, ARA&A, 55, 433
Kaspi Y., Showman A. P., 2015, ApJ, 804, 60
Kasting J. F., 1991, Icarus, 94, 1
Kasting J. F., Pollack J. B., Crisp D., 1984, J. Atmos. Chem., 1, 403
Kasting J. F., Whitmire D. P., Reynolds R. T., 1993, Icarus, 101, 108
Kasting J. F., Kopparapu R., Ramirez R. M., Harman C. E., 2014, Proc. Natl. Acad. Sci., 111, 12641
Kiehl J. T., Hack J. J., Bonan G. B., Boville B. A., Williamson D. L., Rasch P. J., 1998, J. Clim., 11, 1131
King M. D., Platnick S., Menzel W. P., Ackerman S. A., Hubanks P. A., 2013, IEEE Trans. Geosci. Remote Sens., 51, 3826
Kirschvink J., 1992, The Proterozoic Biosphere: A Multidisciplinary Study. Cambridge Univ. Press, Cambridge, p. 51
Kitzmann D., 2017, A&A, 600, A111
Kokhanovsky A., 2021, Front. Environ. Sci., 9, 757575
Koll D. D. B., Malik M., Mansfield M., Kempton E. M.-R., Kite E., Abbot D., Bean J. L., 2019, ApJ, 886, 140
Komacek T. D., Abbot D. S., 2019, ApJ, 871, 245
Kopparapu R. K. et al., 2013a, ApJ, 765, 131
Kopparapu R. K., Ramirez R., Kasting J. F., 2013b, ApJ, 770, 82
Kopparapu R. K., Ramirez R. M., SchottelKotte J., Kasting J. F., Domagal-Goldman S., Eymet V., 2014, ApJ, 787, L29
Kreidberg L., 2018, Exoplanet Atmosphere Measurements from Transmission Spectroscopy and Other Planet Star Combined Light Observations. Springer International Publishing, Cham, p. 2083
Kuell V. et al., 2005, J. Geophys. Res.: Atmos., 110, D16104
Kunze M., Godolt M., Langematz U., Grenfell J. L., Hamann-Reinus A., Rauer H., 2014, Planet. Space Sci., 98, 77
Leconte J., Forget F., Charnay B., Wordsworth R., Pottier A., 2013, Nature, 504, 268
Leconte J., Wu H., Menou K., Murray N., 2015, Science, 347, 632
Loeb N. G. et al., 2018, J. Clim., 31, 895

[24]https://nexss.info/

Lovelock J. E., 1965, Nature, 207, 568

McKay C. P., 2014, Proc. Natl. Acad. Sci., 111, 12628

Maiolino R. et al., 2013, preprint (arXiv:1310.3163)

Malik M. et al., 2017, AJ, 153, 56

Malik M., Kitzmann D., Mendonça J. M., Grimm S. L., Marleau G.-D., Linder E. F., Tsai S.-M., Heng K., 2019, AJ, 157, 170

Manabe S., Wetherald R. T., 1967, J. Atmos. Sci., 24, 241

Meadows V. S., Barnes R. K., 2018, Factors Affecting Exoplanet Habitability. Springer International Publishing, Cham, p. 2771

Meredith M. P., Brandon M., 2017, Sea Ice, 3rd edn., John Wiley & Sons, Chichester, p. 216

Mlawer E. J., Taubman S. J., Brown P. D., Iacono M. J., Clough S. A., 1997, J. Geophys. Res., 102, 16,663

Mlawer E. J., Payne V. H., Moncet J. L., Delamere J. S., Alvarado M. J., Tobin D. C., 2012, Phil. Trans. R. Soc. A, 370, 2520

Morley C. V., Kreidberg L., Rustamkulov Z., Robinson T., Fortney J. J., 2017, ApJ, 850, 121

Murante G. et al., 2020, MNRAS, 492, 2638

Myhre G., Highwood E. J., Shine K. P., Stordal F., 1998, Geophys. Res. Lett., 25, 2715

Nissen K. M., Matthes K., Langematz U., Mayer B., 2007, Atmos. Chem. Phys., 7, 5391

North G. R., Coakley J. A. Jr., 1979, J. Atmos. Sci., 36, 1189

North G. R., Cahalan R. F., Coakley J. A., Jr., 1981, Rev. Geophys. Space Phys., 19, 91

Payne R. E., 1972, J. Atmos. Sci., 29, 959

Perrin M. Y., Hartmann J. M., 1989, J. Quant. Spectrosc. Radiat. Transfer, 42, 311

Pierrehumbert R. T., 2010, Principles of Planetary Climate. Cambridge Univ. Press, Cambridge (P10)

Provenzale A., 2014, Rend. Lincei, 25, 49

Quanz S. P. et al., 2021, preprint (arXiv:2101.07500)

Ramirez R. M., Kaltenegger L., 2018, ApJ, 858, 72

Ramirez R. et al., 2019, BAAS, 51, 31

Rauer H. et al., 2014, Exp. Astron., 38, 249

Reiners A., Basri G., Browning M., 2009, ApJ, 692, 538

Richard F. J., 1959, J. Exp. Bot., 10, 290

Ricker G. R. et al., 2015, J. Astron. Telesc. Instrum. Syst., 1, 014003

Rogers L. A., 2015, ApJ, 801, 41

Rothman L. S. et al., 1992, J. Quant. Spectrosc. Radiat. Transfer, 48, 469

Rushby A. J., Shields A. L., Joshi M., 2019, ApJ, 887, 29

Schwieterman E. W. et al., 2018, Astrobiology, 18, 663

Seidel D. J., Ross R. J., Angell J. K., Reid G. C., 2001, J. Geophys. Res., 106, 7857

Selsis F., Kasting J. F., Levrard B., Paillet J., Ribas I., Delfosse X., 2007, A&A, 476, 1373

Shields A. L., 2019, ApJS, 243, 30

Shields A. L., Meadows V. S., Bitz C. M., Pierrehumbert R. T., Joshi M. M., Robinson T. D., 2013, Astrobiology, 13, 715

Shields A. L., Bitz C. M., Meadows V. S., Joshi M. M., Robinson T. D., 2014, ApJ, 785, L9

Silva L., Vladilo G., Schulte P. M., Murante G., Provenzale A., 2017a, Int. J. Astrobiol., 16, 244

Silva L., Vladilo G., Murante G., Provenzale A., 2017b, MNRAS, 470, 2270

Simonetti P., Vladilo G., Silva L., Maris M., Ivanovski S. L., Biasiotti L., Malik M., von Hardenberg J., 2022, ApJ, 925, 105

Snellen I. et al., 2015, A&A, 576, A59

Spiegel D. S., Menou K., Scharf C. A., 2008, ApJ, 681, 1609

Stringer W., Groves J., 1991, Arctic, 44, 164

The LUVOIR Team, 2019, preprint (arXiv:1912.06219)

Thompson S. L., Barron E. J., 1981, J. Geol., 89, 143

Tinetti G. et al., 2018, Exp. Astron., 46, 135

Trenberth K. E., Caron J. M., 2001, J. Clim., 14, 3433

Udry S., Santos N. C., 2007, ARA&A, 45, 397

Vladilo G., Hassanali A., 2018, Life, 8, 1

Vladilo G., Murante G., Silva L., Provenzale A., Ferri G., Ragazzini G., 2013, ApJ, 767, 65 (V13)

Vladilo G., Silva L., Murante G., Filippi L., Provenzale A., 2015, ApJ, 804, 50 (V15)

Von Paris P., Selsis F., Kitzmann D., Rauer H., 2013, Astrobiology, 13, 899

Walker J. C. G., Hays P. B., Kasting J. F., 1981, J. Geophys. Res., 86, 9776

Wiedner M. C. et al., 2021, Exp. Astron., 51, 595

Wild M., Folini D., Schär C., Loeb N., Dutton E. G., K"onig-Langlo G., 2013, AIP Conf. Proc., 1531, 628

Williams D. M., Kasting J. F., 1997, Icarus, 129, 254 (WK97)

Winn J. N., Fabrycky D. C., 2015, ARA&A, 53, 409

Wolf E. T., Toon O. B., 2013, Astrobiology, 13, 656

Wolf E. T., Toon O. B., 2014, Geophys. Res. Lett., 41, 167

Wolf E. T., Toon O. B., 2015, J. Geophys. Res.: Atmos., 120, 5775

Wolf E. T., Kopparapu R., Haqq-Misra J., Fauchez T. J., 2022, Planet. Sci. J., 3, 7

Wordsworth R., Forget F., Eymet V., 2010, Icarus, 210, 992

Yang J., Boué G., Fabrycky D. C., Abbot D. S., 2014, ApJ, 787, L2

Yang J. et al., 2016, ApJ, 826, 222

Yang H., Komacek T. D., Abbot D. S., 2019, ApJ, 876, L27

Zhao Z., Liu Y., Li W., Liu H., Man K., 2021, ApJ, 910, L8

This paper has been typeset from a TeX/LaTeX file prepared by the author.